NRC·CNRC

NRC Publications Archive
Archives des publications du CNRC

Civil Aviation Alternate Fuels Contrails and Emissions from high-Blend Biofuels (CAAFCEB): contrails analysis

Brown, A. P.; Bastian, M.; Canteenwalla, P.

For the publisher's version, please access the DOI link below./ Pour consulter la version de l'éditeur, utilisez le lien DOI ci-dessous.

Publisher's version / Version de l'éditeur:

https://doi.org/10.4224/40001409

Laboratory Technical Report (National Research Council of Canada. Flight Research Laboratory); no. LTR-FRL-2018-0029, 2018-03

NRC Publications Archive Record / Notice des Archives des publications du CNRC :

https://nrc-publications.canada.ca/eng/view/object/?id=8f448872-70de-4fa9-b150-af0e278c6e69

https://publications-cnrc.canada.ca/fra/voir/objet/?id=8f448872-70de-4fa9-b150-af0e278c6e69

Access and use of this website and the material on it are subject to the Terms and Conditions set forth at https://nrc-publications.canada.ca/eng/copyright

READ THESE TERMS AND CONDITIONS CAREFULLY BEFORE USING THIS WEBSITE.

L'accès à ce site Web et l'utilisation de son contenu sont assujettis aux conditions présentées dans le site https://publications-cnrc.canada.ca/fra/droits

LISEZ CES CONDITIONS ATTENTIVEMENT AVANT D'UTILISER CE SITE WEB.

Questions? Contact the NRC Publications Archive team at PublicationsArchive-ArchivesPublications@nrc-cnrc.gc.ca. If you wish to email the authors directly, please see the first page of the publication for their contact information.

Vous avez des questions? Nous pouvons vous aider. Pour communiquer directement avec un auteur, consultez la première page de la revue dans laquelle son article a été publié afin de trouver ses coordonnées. Si vous n'arrivez pas à les repérer, communiquez avec nous à PublicationsArchive-ArchivesPublications@nrc-cnrc.gc.ca.

National Research Council Canada | Conseil national de recherches Canada

Canada

NRC·CNRC Aerospace

Civil Aviation Alternate Fuels Contrails and Emissions from high-Blend Biofuels (CAAFCEB) – Contrails Analysis

LTR-FRL-2018-0029

A P Brown, M Bastian, P Canteenwalla

Flight Research Laboratory

March 2018

National Research Council Canada | Conseil national de recherches Canada

Canada

Table of Contents

ABSTRACT

Over the period October 2017 to March 2018, the project Civil Aviation Alternate Fuels Contrails and Emissions with high Blend Biojet (CAAFCEB) was undertaken by the NRC, under sponsorship of Environment & Climate Change Canada, Transport Canada, Lanza Tech and the NRC. The NRC Falcon undertook flight operations on Jet A1, JP-5 (in particular, fuel 'A-3' of the North American Jet Fuel Combustion Program, NJFCP, and LanzaTech ATJ bio-jet. High altitude cruising flight contrails at typical air transport cruise Mach Number of 0.8 (M0.8) were sought for each flight, with engines at maximum continuous thrust (MCT). In cruise, contrails and emissions data was measured by the NRC CT-133 research aircraft, out to 50 km (4 minutes age) length contrails. This was sufficient length to identify the state of contrails, persistent or sublimating, as dictated by background atmospheric conditions – both states were encountered upon CAAFCEB flights. CT-133 measurements consisted of contrail ice particle size and number, particulate and gaseous emissions from the Falcon in cruise.

The LT PNNL fuel was blended *a priori* by the NRC, with 8% Exxon Mobil Solvesso 150 ND mono-aromatics, in order to condition the fuel satisfactorily for the Falcon fuel system. Four LT PNNL fuel flights and two JP-5 flights were undertaken. Fuel samples were taken, from the port wing-tank (Jet A1) and the starboard engine fuel feeder tank (experimental fuel, either LT PNNL ATJ, or A-3 JP-5), for each CAAFCEB flight. Prior to the M0.8 cruising flight contrails on baseline and test fuels sequentially, M0.6 Jet A1 contrails were near/at top-of-climb, at contrail lengths of 0.3-3 km (ages of 0.03-0.30 minutes) at approximately 60% of the fuel-flow of M0.8 contrails. Particulate and gaseous emissions were measured, simultaneously with contrail measurements. Top-of-climb emissions were also measured in dry air (prior to the formation of contrails). All contrails were generated by the NRC Falcon, with the same engines. Individual engine emissions and ice particle formation were not measured. Rather, the wake and contrail cross-sections were measured holistically, over the full vertical and lateral extents. A number of lateral/vertical transects, typically nine, were concatenated in the line-of-flight (contrail axis) direction to form re-constructed contrails.

Aggregated power-law parameter identification has been conducted to account for the effects of varying atmospheric background conditions (of RH over ice, RH lapse rate and air temperature) upon contrail ice particle numbers, for LT PNNL and Jet A1 fuels. These identifications have been used to adjust contrail ice particle number and size to the same reference atmospheric conditions, for each fuel type. The optical properties of extinction and effective particle size (properties that govern the global warming effects of contrails, by the processes of radiative forcing). Compared to Jet A1, particulate emissions from the LT PNNL fuel were reduced 80-90%: aerosols (>10 nano-m) by 82%, ultrafine particles (>2.5 nano-m) by 90% and non-volatiles (>2.5 nano-m) by 81%. Although greatly reduced in number, soot (essentially, non-volatile) particles were sufficient in number nevertheless, for the emissions environment to be categorised, for contrail production, as soot-rich. Contrail ice particle production was lessened proportionately to the reduction in soot particle number. Ice particle sizes did not vary significantly between fuels.

Addressing radiative forcing characteristics, a new parameter has been introduced, namely the Apparent Emission Index of Extinction (AEI_{EX}), defined as the lateral integrand of optical depth of a contrail cross-section, when fully measured at any longitudinal point of its length. This is from the CT-133 data, under the assumption of particle sphericity (measured data

implies the development of non-sphericity >20 km contrail length), for ice particles >0.5µm in size. Data shows significant reduction in AEI_{EX} for LT PNNL, *c.f.* Jet A1. Therefore, the present data are evidence of the desirability to holistically measure AEI_{EX} for the complete contrail ice particle spectra, i.e. *all* ice particle sizes and shapes. This can be achieved by equipping the CT-133 with the ECCC extinction probe, for additional flights.

Classification: Unclass
Distribution: Unlimited

ABBREVIATIONS

AEC_{ZY}	Apparent emission index of the lateral integrand of contrail optical depth (OD), m/kg of fuel burned
AEIm	Apparent emission index of contrail ice particle mass (assuming sphericity), μg/kg of fuel burned
AEIn	Apparent emission index of contrail ice particle number, #/kg of fuel burned
ATJ	Alcohol-to-jet biofuel
BC	Black carbon particles (soot)
CAAFCEB	ECCC/TC/NRC project Civil Aviation Alternate Fuel Contrails and Emissions at high-Blend Biofuel (present project)
CAAFCER	GARDN project Civil Aviation Alternate Fuel Contrails and Emissions Research, funded by GARDN, with enabling In-kind contributions from consortium members, notably Air Canada
c.f.	*confer/conferatu*, Latin meaning 'compared with'
CN	Condensation nuclei
CPC	Condensation particle counter
Cs	Cirro-stratus, high altitude stratified cloud
DAS	Data acquisition system
EDR	Eddy dissipation rate, a representative integrand over spatial-frequency of the atmospheric turbulence power spectra
EIm	Emission Index by mass per kg fuel burned
EIn	Number Emission index by number per kg of fuel burned
FA20	NRC Falcon 20 research jet
FIRNS	FRL inertial reference and navigations system (integrated HG1700 IMU, Novatel GPS and DRP system)
FL	Flight level – pressure altitude, referenced to 1013.25 hPa.
FMS	Flight management system
FSSP-100	Forward scattering spectrometric probe
GFS	Global Forecasting System NWM
GW	Global warming
HAARC	NRC High altitude atmospheric research capability
HEFA	Hydro-processed Esters and Fatty Acids
LoF	Line of flight direction (*i.e.*, parallel to the contrail axis)
LT PNNL	Lanza Tech ethanol-derived ATJ bio-jet fuel
LVW	Lower viscous wake (wake regime below the TWV)
M	Mach Number
MCT	Maximum continuous thrust setting
MED	Median effective diameter (50^{th} percentile of the cumulative volumetric spectrum) of each size-number ice particle spectrum of the FSSP-100 measurements, recorded at 10 spectra per second.
NJFCP	North American Jet Fuel Combustion Program
NRC	National Research Council of Canada
N_1	Engine gas generator rotational speed (%)
nvPM	Non-volatile particulate matter (such as black carbon)
NWM	Numerical weather model
OD	Contrail optical depth, the vertical integrand of contrail extinction coefficients (km^{-1}); thus, OD is non-dimensional.

Classification: Unclass
Distribution: Unlimited

P_S	Atmospheric static air pressure
P_T	Atmospheric total air temperature
RAP	Regional Aviation Product NWM
RF	Radiation forcing (by cloud processes)
RH	Relative humidity
RHi	RH over ice
SNR	Signal-to-noise ratio
TGT	Engine turbine gas temperature (°C)
TKE	Turbulent kinetic energy, $\sqrt{(u'^2+v'^2+w'^2)}$
TOPC	Top of climb
T_S	Static air temperature (Celsius)
TWV	Trailing wake vortex
UJW	Upper jet wake; generally the UJW in cross-sectional shape is a '**T**', the lateral being the UJW crown, the vertical being the UJW stem, and the foot being the TWV region.
UTLS	Upper troposphere lower stratosphere
vPM	Volatile particulate matter
WVap	Water vapour
u'	Unsteady wind component (notably, trailing vortex-induced) in the x direction
v'	Unsteady wind component in the y direction
w'	Unsteady wind component in the z direction
[x]	Line-of-flight axis direction (upstream is positive)
[y]	Lateral direction (to the right is positive, looking upstream)
[z]	Normal direction (upwards is positive)
α_{DP}	α (incidence or angle-of-attack) probe differential pressure

Classification: Unclass
Distribution: Unlimited

1. INTRODUCTION

1.1 Overview

1.1.1 Since late 2011, the NRC has undertaken flight measurements of Heavy Category jet transport aircraft emissions, whilst cruising in the UTLS, covering a variety of older and contemporary aircraft types of >136 metric tonne in weight. The NRC has undertaken contrail measurements since early 2014, surveying contrails generated by Heavy Category jets, including the NASA DC-8, and Medium Category jets, including Air Canada A320 jet contrails and those generated by Falcon 20 jets of the NRC, NASA and DLR.

1.1.2 NASA DC-8 and NRC Falcon 20 (FA-20) emissions measurements have emphasised biofuel flight research. Emissions from biofuels of HEFA-blends (43%, 50% and 60% with Jet A1, 50% with Jet A), CH (100% ARA ReadiJet), HEFA-SPK (Shell Virent) and presently, ATJ (92% LT PNNL-PNNL, 8% aromatics, 150 ND) have been measured, Contrails generated by the NASA DC-8 on 50% HEFA-blend, and the NRC Falcon on 60% HEFA-blend, HEFA-SPK (Shell Virent) and presently, ATJ (92% LT PNNL-PNNL with 8% aromatics, 150 ND) have been measured,

1.1.3 In the present project, contrails from LT PNNL ATJ and JP-5 (NAJFCP fuel 'A-3') have been measured by the NRC CT-133 research jet, equipped with a range of sensor instrumentation.

1.2 Background

1.2.1 For young contrails (herein defined as contrails of an age range of 0-5 minutes), covering the contrail states from generation to persistence (defined as a non-negative lapse-rate of AEIn with contrail length) , characteristics are dominated by trailing vortices, which induce extremely high magnitudes and gradients of vorticity, in comparison to any background atmospheric vorticity state [2]. The high gradients dominate young contrail characteristics, such that the cross-plane ([lateral vertical] plane) is dominant, in studying the nature and characteristics of young contrails, as they transition to persistent, or sublimating, contrails.

1.2.2 Therefore, NRC data analysis of flight emissions and contrails has been centred upon the contrail and emissions cross-plane. By holistically re-constructing this cross-plane from a number of transects obtained in the LoF direction [3]. This spatiotemporal analytical reduction methodology has the benefit of being autonomous, thereby obviating any dependency upon an intermediate species, nor upon similarity between plumes of different phase and species.

1.2.3 The NRC contrail data obtained by the NRC CT-133, from the NASA DC-8 contrail, in NASA ACCESS II, indicated [1, 2] a reduction in contrail ice particle number production, using 50% HEFA-blend (with a very low-sulphur Jet A) *c.f.* very low-sulphur Jet A. However, the DC-8 contrails were wake vortex type, dominated by the DC-8 trailing vortices. Very little UJW condensate was present, although UJW contrails from the DC-8 have been

Classification: Unclass
Distribution: Unlimited

previously observed by NASA. Thus, the NRC ACCESS II conclusion on the reduction of contrail ice particle number required extension to UJW contrails. In particular, the St Lawrence Seaway region of south-eastern Canada is dominated by the North American Jetstream. Within this area, UJW contrails are prevalent. The GARDN CAAFCER project measured contrails from Air Canada A320/321 jets in commercial service, operating on Jet A1 and on 43% HEFA-blend. The contrails were dominated by vertical development, due to the strong entrainment effect from closely-spaced trailing vortices [4]. Persistent contrails on these flights included UJW-crown lateral spread, of cirro-cumuliform type by five minutes age. The project demonstrated a reduction in contrail ice particle number for these UJW contrails [4].

1.2.4 The potentially-beneficial effects of reducing the thickness of contrails relate to solar radiation entrapment by persistent contrails, following their transformation to cirrus and lateral spread. The resultant radiation forcing is considered to be a global-warming (GW) driver [5]. Assessment of the magnitude of this potential benefit requires the measurement of the optical effects of contrail spectra, through the full lifetime of formation and persistence, and the effects upon optical characteristics by the widest range of fuel properties, including new generation bio-jet fuels.

1.2.5 As a first step in this regard, the present project, CAAFCEB, has been conducted to provide data for a wide range of hydrogen mass content in jet fuel – by using a JP-5 (low hydrogen content, conversely high carbon mass content) Jet A1 and LanzaTech ethanol-based ATJ bio-jet (high hydrogen content, conversely low carbon content). Contrail ice particle data has been further analysed, in CAAFCEB, to include contrail optical parameters, in accordance with ECCC methodology [6].

2. EXPERIMENTAL DETAILS

2.1 Aircraft and sensor details

2.1.1 The NRC CT-133 is shown with sensors, in the HAARC CAAFCEB configuration, in Figure 1. The aircraft sensor fit has been progressively upgraded since initial commissioning of the CT-133 as HAARC, in late 2011.

2.1.2 Of note in relation to sensor installation upgrades, the Licor 840A forward-facing inlet was modified for inertial separation of ice particles from gaseous (water vapour and CO_2) sensing; this has been generally successful, but occasionally some particular ice crystal shapes are not separated, resulting in an apparently excessive water vapour reading. Thus, the inlet design was modified to a ‘submerged’ sample-air pick-off with inertial separation, for the elimination of contrail ice particles in the sample flow. The bypass action has been generally successful, but on limited occasions the WVap measurements appeared to suffer to some extent, from ice contamination.

2.1.3 The water vapour content (WVap) measurement was used for the calculation of background relative humidity and RH over ice. For the latter, the WVap was combined with static air pressure (Weston Aerospace pressure transducer) and temperature (Rosemount TAT probe) and RHice calculated using the Vaisala method. WVap was compared against numerical weather model forecast soundings and Maniwaki weather balloon soundings, in order to correct for the combination of 840A drift and zero-uncertainty (the former was a

Classification: Unclass
Distribution: Unlimited

limitation of the 840A sensor, the latter was principally due to sample-cell air temperature uncertainty, associated with the forward-facing inlet and lack of volume for full temperature controlling).

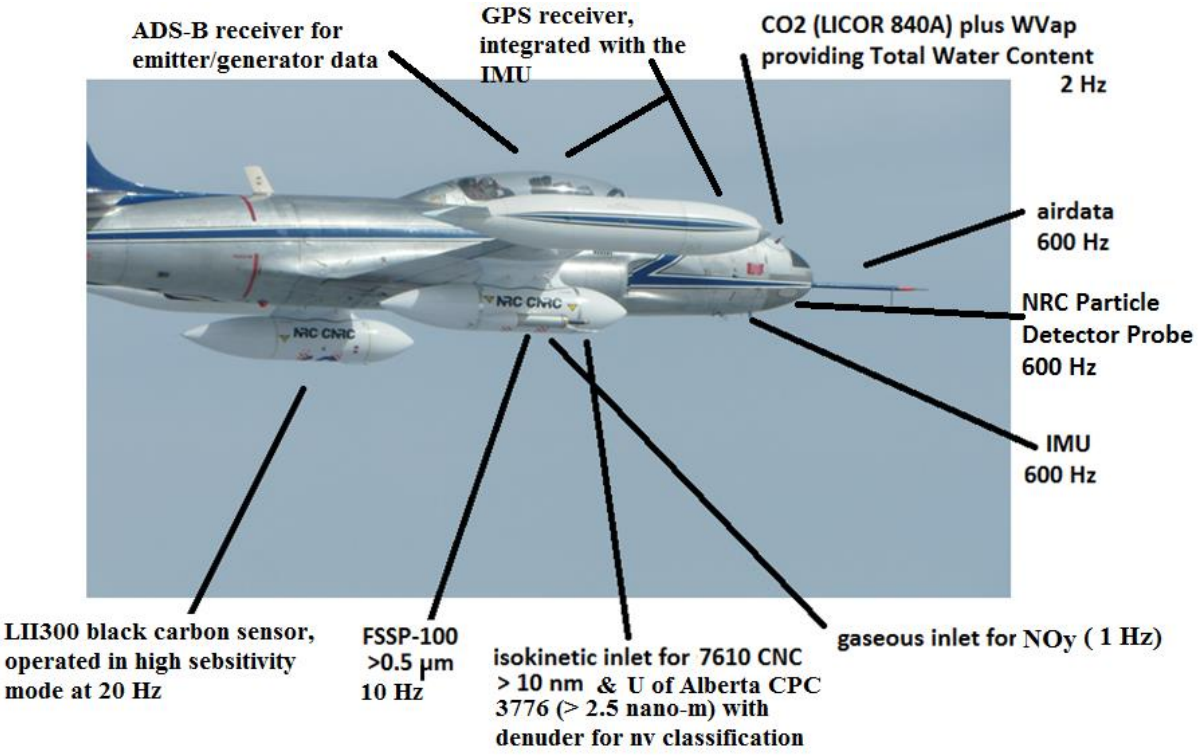

Figure 1, NRC CT-133 research jet, equipped with contrail and emissions measurement sensors for the CAAFCEB configuration (same sensor suite as the CAAFCER GARDN project).

2.1.4 The ECCC FSSP-100 ice particle sensor was mounted on the starboard underwing pod, and co-located with the isokinetic probe supplying the CN and CPC sensors. The FSSP-100 was equipped with Korolev Tips, deflecting shattered ice particles outside the open-flowpath. It was carefully calibrated to sense accurately in the first bin size, ≥0.5µm. Nevertheless, residual uncertainty related principally to measurement sensitivity in the lowest size bin.

2.1.5 BC was initially measured using the LII200. It was upgraded to an LII300 installation in 2015. In contrails, the LII300 appeared to be at times, sensitive to the presence of ice particles. This effect has been observed as an apparent reduction in BC mass concentration and loss of spatial coherence. A possible physical mechanism could be reflective scattering of incident laser energy, to the point of inhibiting atomic resonance of carbon atoms and thus inhibiting incandescence and vapourisation. Thus, as a future upgrade, it is planned to install a denuder upstream of the optical chamber, in order to eradicate ice particles from potentially interfering with the measurement of BC.

2.1.6 Sensors are described in Table 1 and flight details are contained in Table 2. The CPC was coupled with a denuder for non-volatile classification of ultrafine particles. By valve switching, the denuder could be bypassed (providing a measure of total ultra-fines) or it could be switched in-line, upstream of the CPC and thus enabling a measure of non-volatiles. Typically, the denuder was sequentially operated in bypass for two minutes, thence in-line for approximately the same period.

Classification: Unclass
Distribution: Unlimited

Table 1, NRC CT-133 emissions and contrails measurement instrumentation

Sensor location	Sensor	Description	Acquisition rate
Port wing			
Wing surface, outboard	Wing glove, 24 surface pressure sensors	Measures high-rate unsteady aerodynamic forces, for example, during the penetration of trailing vortex cores	600 Hz or 1200 Hz
Under-wing HAARC pod	LII 300 BC sensor	Measuring BC volumetric concentration of mass.	20 Hz
Starboard wing			
Under-wing HAARC pod	CN 7610 aerosol counter	condensation nuclei counter, >10 nano-metres	10 Hz
	CPC 3776 ultrafine aerosol counter	ultrafine aerosol counter, for particles >2.5 nano-metres in size	10 Hz
	Denuder	non-volatile particle path for CPC 3776 (vaporizes volatile particles) – when bypassed CPC 3776 counts volatile and nv.	-
	Thermo 42I	NOx analyser, operated in the streaming mode, hence measuring NOy (majority of young contrail emissions NO, some HONO compounds)	1 Hz
	FSSP-100	Forward-scattering spectrometric probe, measuring particles > 0.5 µm in size – in this environment, ice particles	20 Hz
Nose	Licor 840A	CO2 and water vapour measurement	3 Hz
	FIRNS	Inertial reference & navigation system, based upon the HG1700 IMU, Kalman-filter blended with GPS	600 Hz
	Air data boom	Atmospheric pressure and temperature, pitot pressure; incidence and sideslip angles.	600 Hz
	Particle detector probe (PDP)	Measuring ice particle concentration	20 Hz
Cockpit	Novatel DGPS receiver	GPS	600 Hz
	DAS	Central data acquisition system for all state & sensor parameters	600 Hz
	Line-of-flight video camera	Recording line of flight view (visual spectrum)	60 frames per second

Classification: Unclass
Distribution: Unlimited

Table 2, CAAFCEB flight details

Date	Fuel sequence & contrails			Background atmosphere
20 Nov 17	(1) Jet Al	M0.6	Dry air climb; TOPC contrail measured <3 km	Locally high RH in an area of lateral extent
	(2) Jet Al	M0.8	Contrail visibly sublimated at 22 km length	
	(3) JP-5	M0.8	Contrail sublimated at 16 km length	
28 Nov 17	(1) JetA1	M0.6	Cirrostratus to tropopause; TOPC embedded contrail measured 0-3 km length	Cs widespread; contrails embedded; FSSP did not sense background Cs ice particles
	(2) LT PNNL	M0.77	First LT PNNL operation in high altitude cruise; Embedded contrail measured to 10 km, then definition lost discernment	
	(3) Jet A1	M0.8	Contrail was embedded in background cirrus	
21 Dec 17	(1) Jet A1	M0.6	Lateral extent of high RH 90 km, then contrail dissipated	Strong Jetstream influence; contrails formed in 90 km pool of RH within 160 knot wind.
	(2) Jet A1	M0.8	Searched for and encountered another pool of RH, persistent contrail before fuel changeover	
	(3) LT PNNL	M0.8	Persistent contrail to 50 km length	
	(4) Jet A1	M0.8	After fuel change-back and commencement of descent, contrail then stopped forming	
19 Jan 18	(1) Jet A1	M0.6	TOPC contrail measured 0-3 km length	RH gradually reduced after 100 km lateral extent
	(2) JP-5	M0.8	Persistent, light contrail, fading in sublimation	
	(3) Jet A1	M0.8	Fade-in from sublimating to persistent contrail	
12 Mar 19	(1) Jet A1	M0.6	Sudden contrail onset at FL270 in climb; measured 0-3 km length.	Smaller lateral areas of high RH, 50 km in lateral extent
	(2) LT PNNL	M0.8	Sublimated at 15 km length	
	(3) Jet A1	M0.8	Sublimated at 23 km length	
22 Mar 19 Trail & reverse-track flight profile (see text)	(1) Jet A1	M0.8	Level at FL300, acceleration to M0.8 conducted on JetA1, heading east, persistent contrail	The original JetA1 contrail had transformed to emitter flight level cirrostratus, laterally spread, and thin in depth; AEIn was similar to young stage..
	(2) LT PNNL	M0.8	The FA20 tuned west and changed to LT PNNL, over-flew the CT-133 heading east; LT PNNL contrail to >30 nautical miles, slowly sublimating	
	(3) Jet A1	M0.8	CT-133 flew the reverse track of the FA20 and re-encountered the FA20 earlier JetA1 contrail.	

Classification: Unclass
Distribution: Unlimited

2.2 Weather forecasting

2.2.1 Numerical weather model predictions of UTLS WVap were used for flight decision making. Through the course of the 2017/18 projects, NWM accuracy was assessed by inflight occurrences of cirrus cloud and contrails. In this regard, the GFS NWM was accurate in spring-time conditions, but over-predicted WVap content in winter, 2-300 km to the north of Ottawa, Ontario. On the other hand the RAP NWM under-predicted WVap content in this area.

2.3 Flight and atmospheric details

2.3.1 Table 2 includes a summary of encountered atmospheric conditions and generated contrails. It is seen that a total of six flights were conducted, all with bulk JetA1 as the baseline fuel; two were flown with 'A-3' JP-5 and four with 92% LT PNNL / 8%150ND.

2.3.2 Inflight images from the CT-133 LOF video camera are shown in Figure 2, three of which are video stills from the first LanzaTech (LT PNNL) flight on the 28th November 2017: (a) is a Jet A1 contrail image, at FL320 near TOPC, with an insert image of the Falcon from below: this image is instructional in showing the distance from the engine exit planes (black discs near the aircraft tailplane/fin) to the onset of a visible contrail – as shown, the distance was approximately 1.3 wingspans; the contrail, at 0.5 km length is dominated by the roll-up of shed vorticity from wing bound circulation into a pair of trailing vortices – seen from below, the contrail had a U-shape to it.

2.3.3 Image (b) was taken during fuel changeover at M0.6, from Jet A1 to LT PNNL, the contrail length was approximately 0.2 km. Images (c) and (d) were for two-engine operation of the Falcon on LT PNNL fuel, with engines at MCT: (c) M0.68, contrail length was approximately 0.7 km; (d) CT-133 flying reverse track, at intercept and then approximately 50 km length, contrail nearly invisible.

(a) (contrast and brightness adjusted, for contrail delineation) (Figure 2 continued over-page, with caption)

Classification: Unclass
Distribution: Unlimited

(b)

(c) (image brightness and contrast adjusted) **(Figure 2 continued over-page, with caption)**

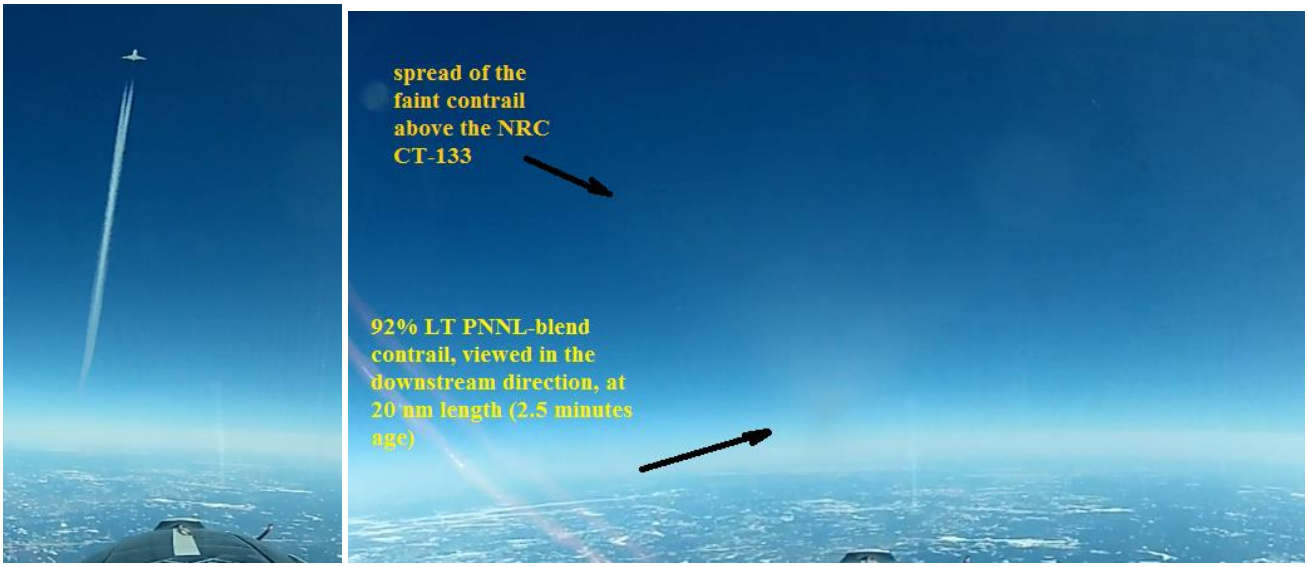

(d)

Figure 2 – still images from CT-133 LOF video camera (note background atmospheric cirrus, present to the tropopause):- (a), Jet A1 contrail at M0.6 near TOPC; (b), contrail during changeover to LT PNNL steady at M0.6 (700 lb/hr/engine fuel-flow); (c) two-engine operation on LT PNNL, M0.7 during acceleration to M0.8 (fuel-flow ≈1200 lb/hr/engine during acceleration); (d) reverse-track flight profile, 1,000 feet below the FA20 on a head-on pass (*left*), then the CT-133 climbed to contrail-level on the reverse track (*right*), very faint, almost invisible contrail at 50 km length.

2.3.4 Particularly evident in the forming contrail (Figure 2(c)), in the top-left of the image, are helical striations of condensate around each of the trailing vortices at the base of the contrail; these were evidence of the entrainment of free shear-layer shed vorticity from wing and fuselage boundary layer (orthogonal in plane to the vorticity of the trailing vortex pair) and the interaction between the exhaust jet-flow vorticity and the rolling-up trailing vorticity. Such features were not associated with the type of fuel powering the engines.

2.4 Flight profile descriptions

2.4.1 Unique to NRC flight research operations for the autonomous and holistic measurement of contrails, two flight profile types were flown by the FA20 / CT-133 pair of aircraft, as described below:

a. ***Flights 1-5:*** line-astern, same track method, optimised for measurement of young contrails (0-5 minutes in age): the CT-133 flew behind the FA20, on the same heading; low amplitude weaving was conducted, to cross the emissions plume (in clear air) or the contrail (when contrailing) in a continuous series of lateral and vertical traverses, the extremities of each traverse were in background atmospheric conditions; when the optimum contrail formation altitude was determined, the FA20 accelerated to M0.8, the maintenance of which required nominally MCT; on Flights 2-5, this was conducted following changeover to the experimental fuel (either A-3, a low-sulphur JP-5, or LT PNNL ethanol ATJ-derived biojet); when 100-140 km ahead, the FA20 entered a reverse-turn , changing to the baseline fuel; the CT-133 did likewise ahead of the FA20, re-intercepting the FA20 from below, then measuring the contrail behind the FA20, from the opposing fuel;

b. ***Flight 6:*** reverse track flight profile, optimised for the measurement of ageing, persistent contrails (>15 minutes in age); the baseline (jetA1) contrail was firstly measured as

Classification: Unclass
Distribution: Unlimited

a young contrail, using the line-astern, same track flight method (of Flights 1-5); the CT-133 then broke-off line-astern and orbited clear of the contrail, whilst the FA20 continued track, finally reversing direction in a wide turn, during which it changed to LT PNNL fuel; at this time, the CT-133 established a head-on pass from below, at an aircraft separation of approximately 170 km; as the FA20 passed overhead, the CT-133 promptly climbed into the LT PNNL contrail and measured it in the reverse-track direction (opening at a high rate, approximately 26 kilometres per minute); on this particular flight, the LT PNNL contrail slowly sublimated over a contrail distance of 60-80 km, beyond which it was not possible to visually track the contrail); the CT-133 continued on the reverse track of the FA20, until it re-encountered the JetA1 contrail, which was in a thin, lateral spread state at emitter flight level; Figure 2(d) presents inflight video-stills of the intercept and down-track contrail.

3. FLIGHT RESULTS & DISCUSSION

3.1 Falcon engine operating conditions

3.1.1 The Falcon was essentially operated in two experimental conditions, one relating to in-trail climb (M0.6, FL250-320), and the other relating to high-speed cruise (M0.8 within the altitude FL280-340).

3.1.2 At M0.6, the engines were operating at an endurance thrust setting, with fuel-flows of 600-900 lb/hr/engine, and exhaust gas temperatures of 500-560°C. At M0.8$\pm$0.02, the engines were operated at MCT with fuel-flows of 900-1800 lb/hr/engine and EGT of 650-720°C. Variations were associated with differing Mach Number and cruise altitudes – fuel-flow reduced at higher altitude, whilst EGT increased. As such, intermediate, but nevertheless representative, Mach Numbers were flown, such as the first LT PNNL flight, M0.77 at FL350, fuel-flows 850 lb/hr/engine and EGT 630°C.

3.1.3 Falcon engine operating state was recorded by cockpit video; inertial FIRNS data was recorded on PCMCIA flash-card and post-flight processed. A view of the cockpit video image is shown in Figure 3; (a) shows engine parameters on LT PNNL powered two-engine flight, firstly; (b) then, flight on two-engine Jet A1 operation. There were no sensible differences in engine parameter values, within gauge steadiness parameters.

3.2 Atmospheric conditions

3.2.1 UTLS atmospheric conditions have an effect upon contrail generation, development and persistence. Particular parameters of influence are the background relative humidity over ice (RHice), air temperature and RH lapse rate (particularly in the trailing vortex wake phase, for the last parameter).

3.2.2 CAAFCEB contrails were obtained at various altitudes within the range FL270-FL350. Air temperatures were within the range -45 to -53°C. Atmospheres were either stratified (such as the background Cs of Figure 2), or occasionally, lightly turbulent. For example, the winds aloft on the 21st December 2017 flight were 160 knots in speed, amidst jet-stream induction, and yet the atmosphere was occasionally-light turbulence only.

Classification: Unclass
Distribution: Unlimited

(a)

(b)

Figure 3 – still images from Falcon cockpit video:- (a), LT PNNL powered two-engine operation, FL350, M0.77; (b) two-engine operation on Jet A1, following change-back from LT PNNL fuel.

3.2.3 The flight area was generally 250 km north of Ottawa. Atmospheric conditions tended to possess pools of humidity of spatial scales 40-60 km in extent. Contrail growth

Classification: Unclass
Distribution: Unlimited

conditions varied down-track, between persistent (for $RHI_{ice} \geq 100\%$) and lightly sublimating (pools of $RH_{ice} < 100\%$)..

3.3 Contrail type and variability

3.3.1 NRC Falcon 20 (FA20) contrails were UJW type, with varying initial downwards entrainment induced by the aircraft's trailing vortices.

3.3.2 CAAFCEB contrails optically varied between lightly-sublimating to persistent. Ages varied between 0.05 and approximately 45 minutes, covering young to aged. As observed in the images of Figure 2, the contrails were spatiotemporally non-homogeneous in shape, in all 3-axes. The helical striations observed in Figure 2 were typical of transport jet contrails, and were the result of vorticity interactions between shed vorticity from wing bound circulation, organised into a trailing vortex pair, fuselage and wing boundary layer vorticity (which was orthogonal in plane, to the vorticity of the trailing vortex pair) and engine exhaust jet-flow vorticity.

3.3.3 On the other hand, downstream, axial gradients within the wake-flow structure and interactions with the background atmosphere, resulted in spatiotemporal variations of contrail paths, including meandering, wandering, mutual instabilities, slanting and 'puffing.'

3.4 Emissions

3.4.1 NOy emissions were measured with the Thermo 42I NOx analyser, whilst CO_2 and water vapour concentrations were measured with the LiCor 840A analyser. Within the experimental error of accuracy of $\pm 20\%$, no significant differences in NOy or CO_2 emissions from different jet fuel types were observed.

3.4.2 Aerosol (CN), ultrafines (CPC) and non-volatiles (CPCnv) were successfully measured for every contrail; likewise for FSSP-100 ice particle spectra. All species were collected at 10 Hz sampling. The contrail analyses have been based upon these and atmospheric parameters.

4. ANALYSIS & DISCUSSION

4.1 Young contrail and emissions analysis methodology

4.1.1 Young contrail and emissions cruise flight data for LT PNNL and petroleum jet fuel (JetA1 and 'A-3' JP-5), has been analysed in the spatiotemporal domain, for which the primary spatial variables of dynamic change were in the lateral and vertical directions, orthogonal to the contrail axis. Contrail and emissions plume cross-sections were re-constructed from concatenated sub-sets of nine passes across the contrail (occupying an elapsed time of, typically, two minutes). An example of flight-path concatenation, used to reconstruct a single contrail cross-section, from nine flight-path segments across the contrail, is shown in Figure 4.

4.1.2 From the concatenations of flight-path traverses in the contrail/plume cross-plane, contours were constructed of the desired species (ice particle number, volume, extinction coefficient or effective optical size; also, CN, CPC, CPCnv, NOy, CO_2, water vapour, or BC

Classification: Unclass
Distribution: Unlimited

mass) using the Matlab® *contour* function, which employed Delauney triangulation. [y z] cross-plane step-wise integration is next used, to integrate the species characteristic over the complete contrail or emission plume cross-section, per metre in the direction of flight. Finally, the integrand was divided by the fuel-burn per metre of air distance *i.e.*, fuel-flow/TAS) to derive at the characteristic EI of species.

4.1.3 This method was applied to the data from Flights 1-5 and the first contrail segment on Flight 6. Examples of re-constructed cross-sections are shown in Figure 5, for contrail and emissions species' plume cross-sections. Whereas, in these examples, contrail characteristics were closely associated with atmospheric background RHice, the aerosol and ultrafine concentrations varied widely over the cross-sections, under strong dynamic entrainment effects from trailing-pair vorticity and engine exhaust jet turbulent vorticity.

4.1.4 Analyses of re-constructed contrail cross-sections can be based under the premise of considering contrail characteristics variations and potential parameterisations with fuel properties and atmospheric properties. The contrail data analysis employed the concept of ice particle number Apparent Emission Number Index (AEIn), as used by Karcher [10]. In this, the concept recognised that ice particle production (at least in the soot-rich region, as discussed also by Moore *et al* [11]) is particularly related to soot particle number emissions, and is thereafter attenuated or amplified by downstream, microphysical processes that are interactive with the background atmosphere.

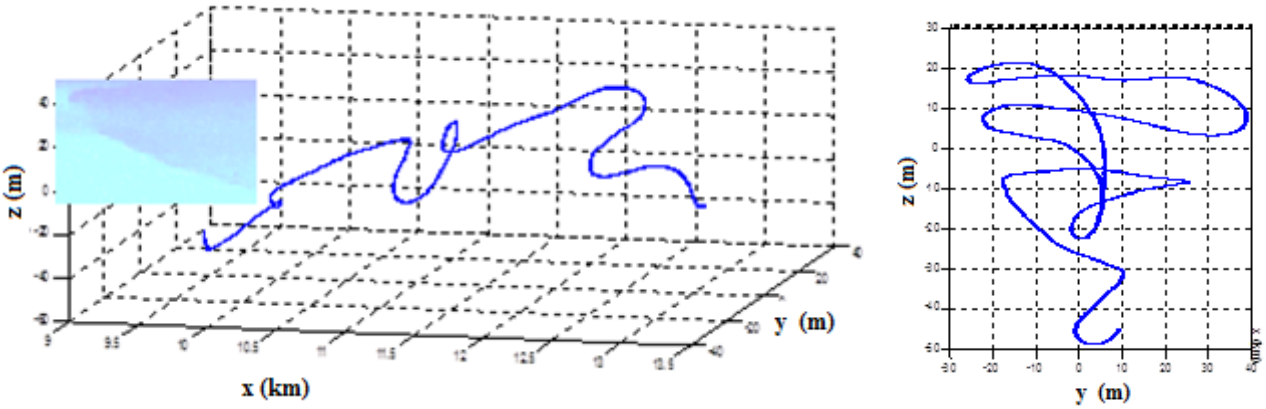

Figure 4, A recorded flight-path segment from the NRC CT-133 during a contrail measurement survey: (*left*), isometric view, predominantly shown along the contrail (x-axis, collinear with the inset contrail photograph), (*right*) end-view, showing the nine flight-path segments across the contrail, from which are re-constructed a single, autonomous cross-section of the contrail.

4.2 Relatively-aged contrail and emissions analysis methodology

4.2.1 When the relatively-aged (*i.e.*, *c.f.* to the young contrail time-frame of 0-5 minutes) JetA1 remnant-contrail was re-encountered on Flight 6, it had transformed to laterally-outspread, wispy cirrostratus cloud at the flight level of the emitter.

Classification: Unclass
Distribution: Unlimited

4.2.2 In this state, it was not possible to fully cover the transformed contrail cross-section. Rather, an intermediary species was used, in this case CN, because of the high remnant concentration (*i.e.*, SNR, *c.f.* to that of CO_2 for example) of that species. EI determination *via* an intermediary, CO_2, has been the customary approach to the measurement of EI in-flight (*e.g.*, [11]).

4.2.3 In all cases (including the present analysis), this approach has been used under an assumption of similarity of species plumes. This assumption has been an approximation to plume(s) responses to the processes of dynamic forcing, diffusion, buoyancy, heat transfer *etc*, involved in ageing. In the present case, the ratio [FSSP-100 ice # concentration] / [CN # concentration] has been used as the intermediary for EI derivation. Assuming similarity, this ratio has been multiplied by CN EIn to derive contrail ice particle AEIn.

4.2.4 For substantiation, this has been bridged-across to actual FSSP AEIn for young contrail cross-sections, by a comparative assessment of the accuracy of the approach for subsequently aged contrail segments. An acceptable accuracy has been demonstrated by this comparison, shown in Figure 6, which also shows the inability to satisfactorily cover the lateral extent of aged-contrail cirrus (due to the wide but thin cross-sectional shape).

4.2.5 Contrail cross-section ice particle spectral median effective diameter (*i.e.*, the MED of each 16-bin FSSP ice particle size spectrum, gathered ten times a second) varied widely (a factor of approximately 4:1) across contrail depth, in particular, and width. Contrail depth was established by trailing vortex-induced downwards entrainment. Each vortex also induced the other downwards, at descent rates of typically 2 m/s. The downwards entrainment involved compressive heating from the atmospheric pressure increase, and could involve descent into drier or more moist air. Hence the RH lapse rate is important for contrail development.

Classification: Unclass
Distribution: Unlimited

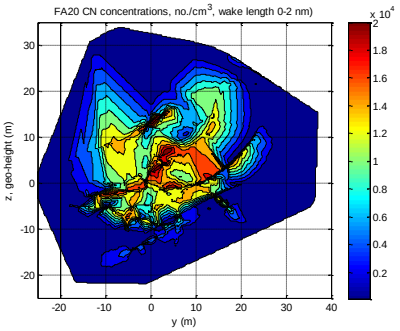

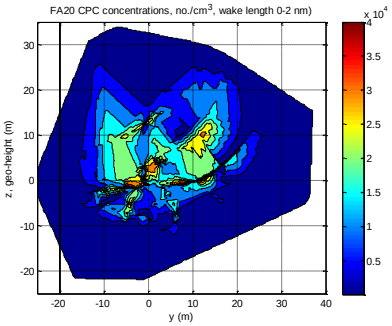

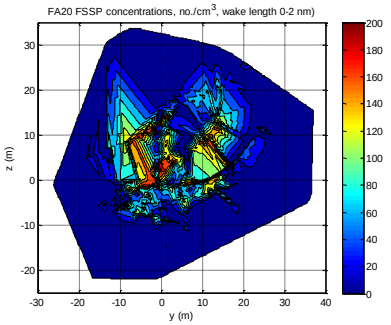

(a) JetA1

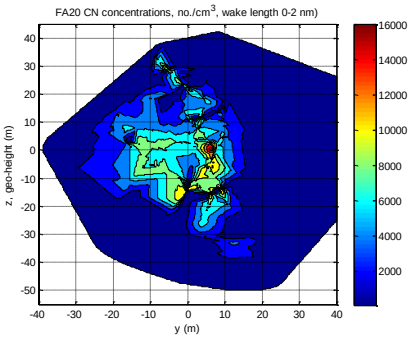

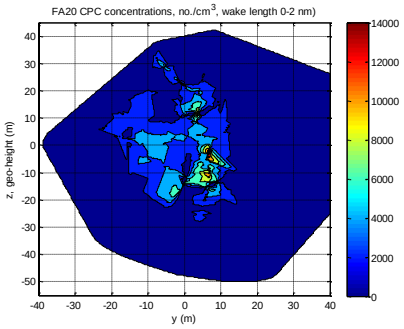

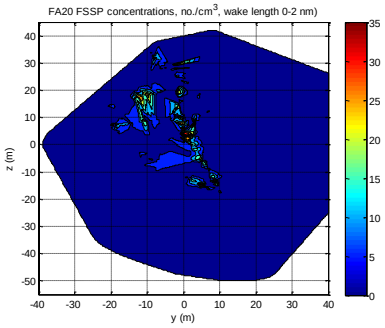

(b) 'A-3' JP-5

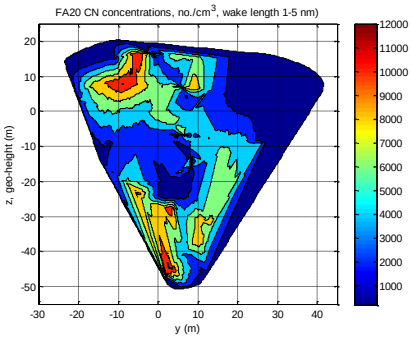

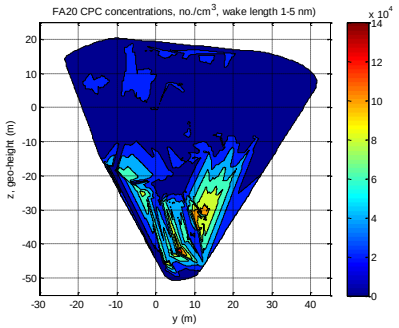

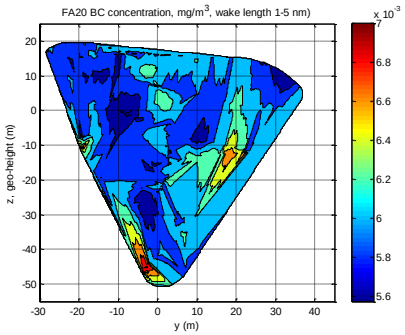

(c) 92% LT PNNL / 8% 150 ND (i)

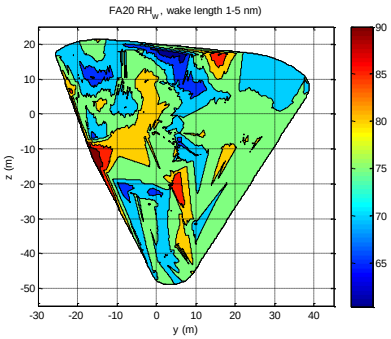

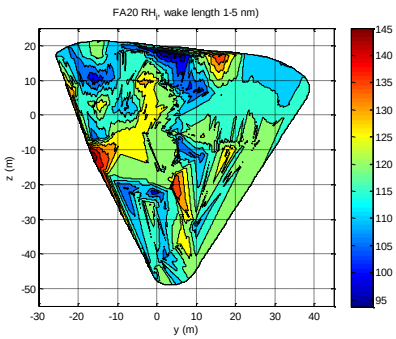

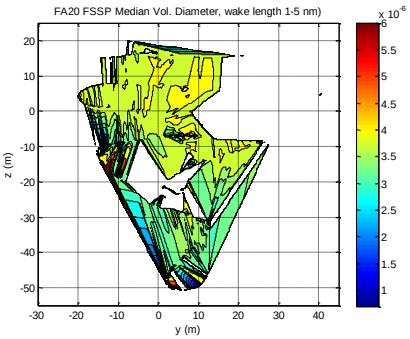

(c) (ii) (continued, with caption, over-page)

Classification: Unclass
Distribution: Unlimited

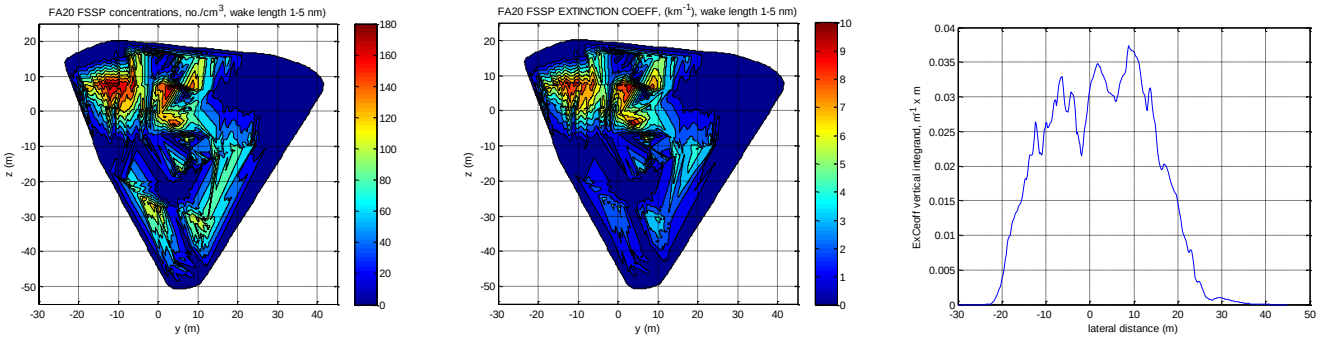

(c) (iii)

Figure 5, examples of re-constructed cross-sections of young contrails and emissions species' plumes, all 2-9 km behind the FA20 generator/emitter: (a) JetA1 example, *(left to right)*, CN, CPC, FSSP-100; (b) 'A-3' JP-5 example, *(left to right)*, CN, CPC, FSSP-100; (c) 92%LT PNNL/8%150 ND example, (i) CN, CPC, BC, (ii) RH, RHice, ice aprticle MED, (iii), ice particle *(left to right)*, number concentration, extinction coeffciient (EC), lateral integrand of EC (defined and explained in the text).

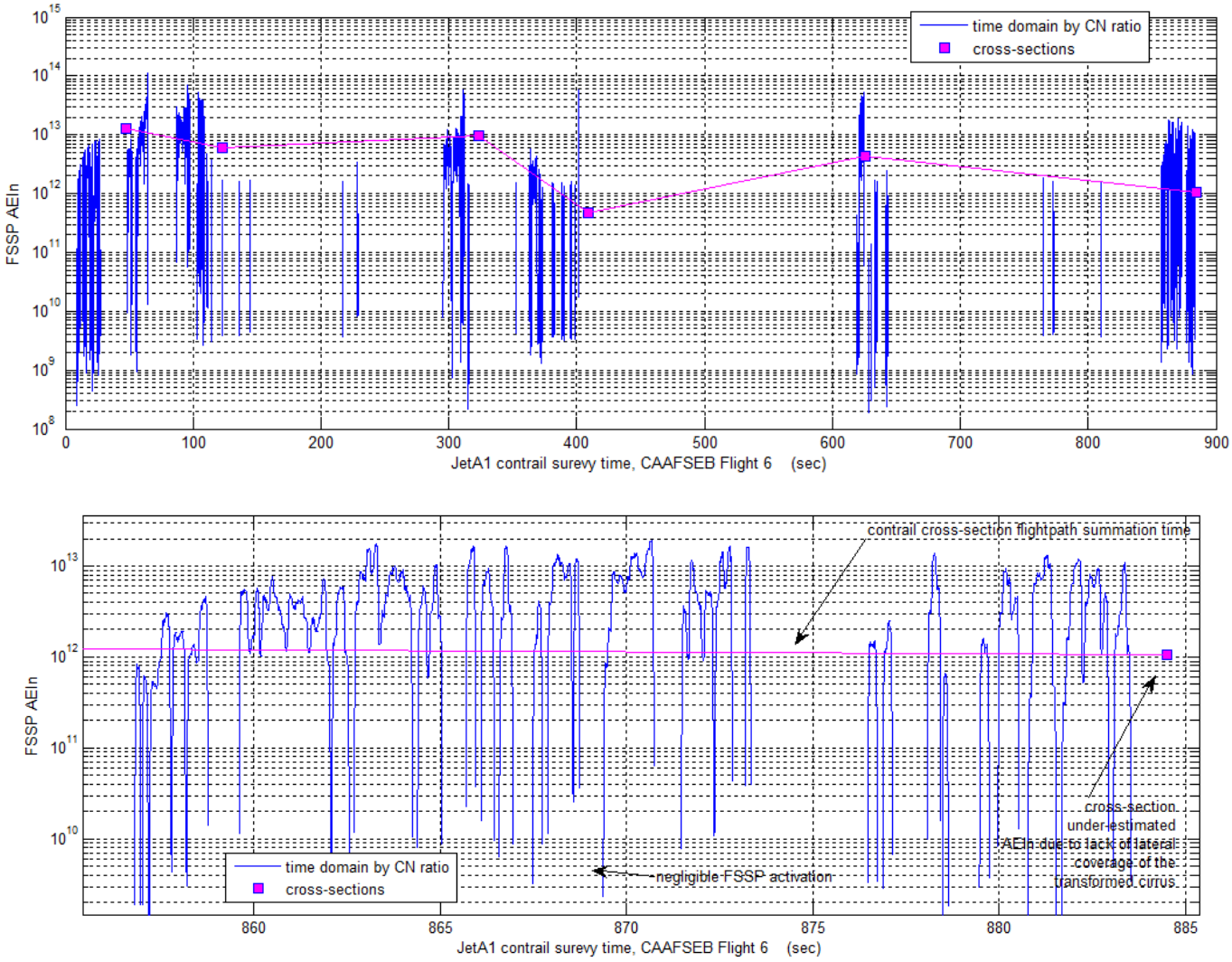

Figure 6 – comparison of aged JetA1 contrail AEIn derivation, 9-segment contrail cross-sectional re-constructions and time-domain [Nconc / CN_conc]*mean(CN EIn), (*top*) complete aged contrail slices, and (*bottom*) close-up view of the final slice.

Classification: Unclass
Distribution: Unlimited

4.3 Fuel properties

4.3.1 Fuel samples were taken from the Falcon for most, although not all, flights. Samples consisted of:

- port wing-tank samples of Jet A1 from a number of flights (all Jet A1 fuel was drawn from the NRC fuel-farm, which has two non-connected in-ground tanks); and,
- starboard engine feeder tank sample of experimental fuel, either 92% LT PNNL blended with 9% ND 150 mono-aromatics, or JP-5.

4.3.2 The fuel-tank samples were be analysed by QETE of DND. In addition, other fuel analyses were available for comparison, including the unblended LT PNNL batch [7], Jet A1 analyses of associated projects [4] and A-3 JP-5 [8]. The properties are summarised in Table 3.

Table 3, Fuel properties, *a priori* projects & analyses and tank sample analyses for CAAFCEB {shaded are Falcon fuel tank samples' analyses, [14]); NOTE: total hydrogen content is presented for NMR test values

Fuel [reference]	Total hydrogen content (%m), mean±1σ	Sulphur content (%m)	Aromatics content (% vol)	Naphthalene (% vol)	Net heat of combustion (MJ/kg)	Density at 15°C (gm/l)
a priori Jet A1 [4]	13.74	0.058	18.3	0.9	43.2	808
Jet A1 [14]	13.85±0.04	0.05	18.5	0.7	43.0	803
LT PNNL [7]	15.33	0.000096	0	-	43.9	761
LT PNNL / 8% 150 ND [14]	14.91±0.15	0.00	8	0.1	43.9	773
A-3 NJFCP [8]	13.7	0.02	18.3			
A-3 JP-5 [14]	13.52±0.06	0.02	20.1	0.9	43.0	827

4.3.3 Of note, the LT PNNL fuel had negligible sulphur content and high hydrogen content. Blending with 8% 150ND Solvesso introduced aromatics (from 0 to 8%). Although Solvesso was specified as mon-aromatics, the tank analyses of LT PNNL / 150ND indicated a minor content of naphthalene, likely introduced by residual feeder tank undrainable fuel (Jet A1) – the feeder tank was not flushed prior to experimental fuel filling. The sulphur, hydrogen and aromatics contents of the Jet A1 were typical, when compared to the *a priori* recent project analyses [4]. JP-5 had relatively low-sulphur (a reduction of 60% *c.f.* JetA1), a 2% reduction in hydrogen content and a 30% increase in naphthalene, *c.f.* Jet A1.

4.3.4 For the A-3 JP-5, the sulphur content reduction (over Jet A1) was significant because CAAFCER contrail data [4] indicated a slight sulphur effect upon contrail ice particle numbers, a direct power-proportionality of $S^{0.55}$ (significant but noticeably less than the production of particles by sulphur content, as indicated in the dry-air flight data of the

Classification: Unclass
Distribution: Unlimited

Aerodyne-NASA sulphur flight experiment [9] for example, for which the volatile particle emissions (vPM) EIn $\propto S^2$ – Figure 7 refers). The correlation could have been due to impurities in sulphate particles, for example tiny soot pieces, enabling activation of the sulphates as ice nuclei. Furthermore, the higher naphthalene content of the A-3 JP-5 could also be expected to increase particle emissions.

4.3.5 Hydrogen content is a strong determining parameter for contrail ice nucleation, due to the relationship between hydrogen content and soot production, for example [8], Figure 7 refers. Soot is a strong ice nucleating attractor, for example considered in detailed contrail microphysical modelling studies by Karcher [10]. ACCESS or CAAFCER contrail AEIn data [4] of the NRC suggested that the A320 contrails (UJW-type) followed a hydrogen relationship, similar to that of Figure 8.

4.4 Contrail ice particles & aerosols emission indices summary

4.4.1 Background atmospheric CPCnv concentrations in the CAAFCEB flight area and altitudes were measured to have been 150-200 ultra-fines per cubic centimetre. CAAFCEB contrail FSSP AEIn data is plotted against CN and CPCnv EIn data, together with that of all contrails measured by the NRC CT-133, in Figure 9. Together with CAAFCER data from Air Canada A320, A321 and B763 aircraft, 2017 [4], the present FA20 AEIn values were the highest measured by the CT-133. Figure 9 includes wide variations in atmospheric conditions (RHice in particular), aircraft types, engine types, individual engine Ser/No, fuel properties and atmospheric conditions. Therefore, as expected, there is also wide variation in measured FSSP AEIn data. Nevertheless, the texture of the data-point spread shows an increasing FSSP AEIn with increasing CN and CPCnv EIn.

4.4.2 Concerning CPCnv in particular, the ratio FSSP AEIn / CPCnv EIn could be expected to represent the activation of soot particles for ice nucleation. It is seen in Figure 9 (bottom) that the maxima values were of the order of 0.10; reasons for this relatively-low value could have included potential non-soot content of CPCnv particles, potential ice particle under-sizing (<0.5 µm, the minimum FSSP-100 sensitivity), potential loss of sensitivity in the minimum-size bin of FSSP-100 spectra, and potential sublimation in descending, compressing air-mass under the action of wake vortex entrainment, particularly with positive RH lapse rate (leading to lower RHice at lower height, also).

4.4.3 Alternatively, CAAFCEB contrail FSSP AEIn data for all variety of test atmospheric conditions, can be simultaneously plotted against EIn data for aerosols, ultra-fines and non-volatiles, CN (>10 nano-m), CPC (>2.5 nano-m) and CPCnv (non-volatile particles, *i.e.*, denuder in-line operation), as presented in Figure 10. This figure has highlighted margins between aerosol and ultra-fine aerosol emissions, for different fuels. For the petroleum fuels, the difference between CN and CPC were large, indicative of large numbers of particles within the size range 2.5-10 nano-m, approximately.

Classification: Unclass
Distribution: Unlimited

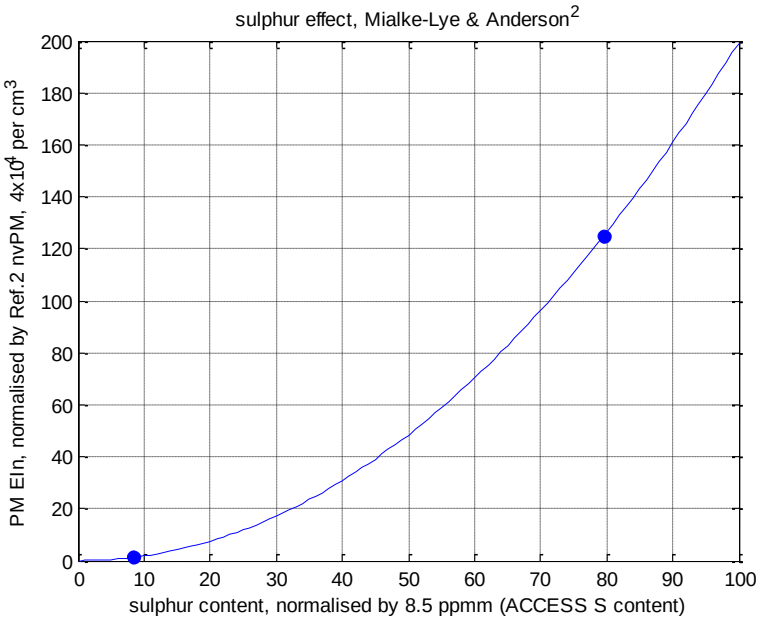

(a)

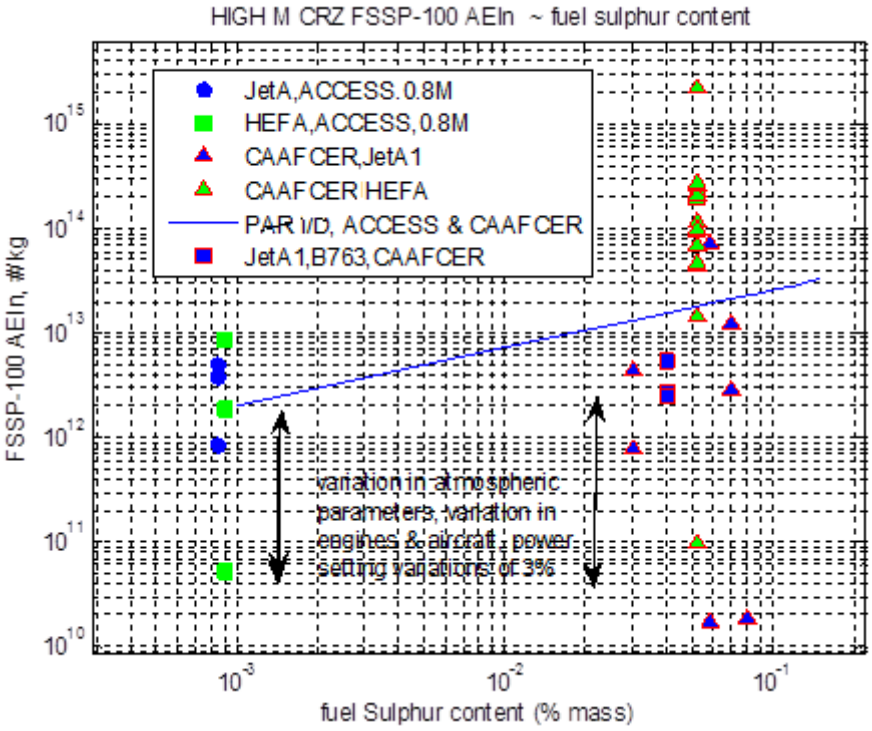

(b)

Figure 7 – *(a)* plot of normalised emitted PM EIn against sulphur content, estimated from Aerodyne/NASA data [9], wherein the curve-fit is second-order, pivoted on the origin, and *(b)* plot of CAAFCER & ACCESS II NRC data of FSSP-100 AEIn against sulphur content, having first adjusted each contrail AEIn for variations in fuel hydrogen content [4].

Classification: Unclass
Distribution: Unlimited

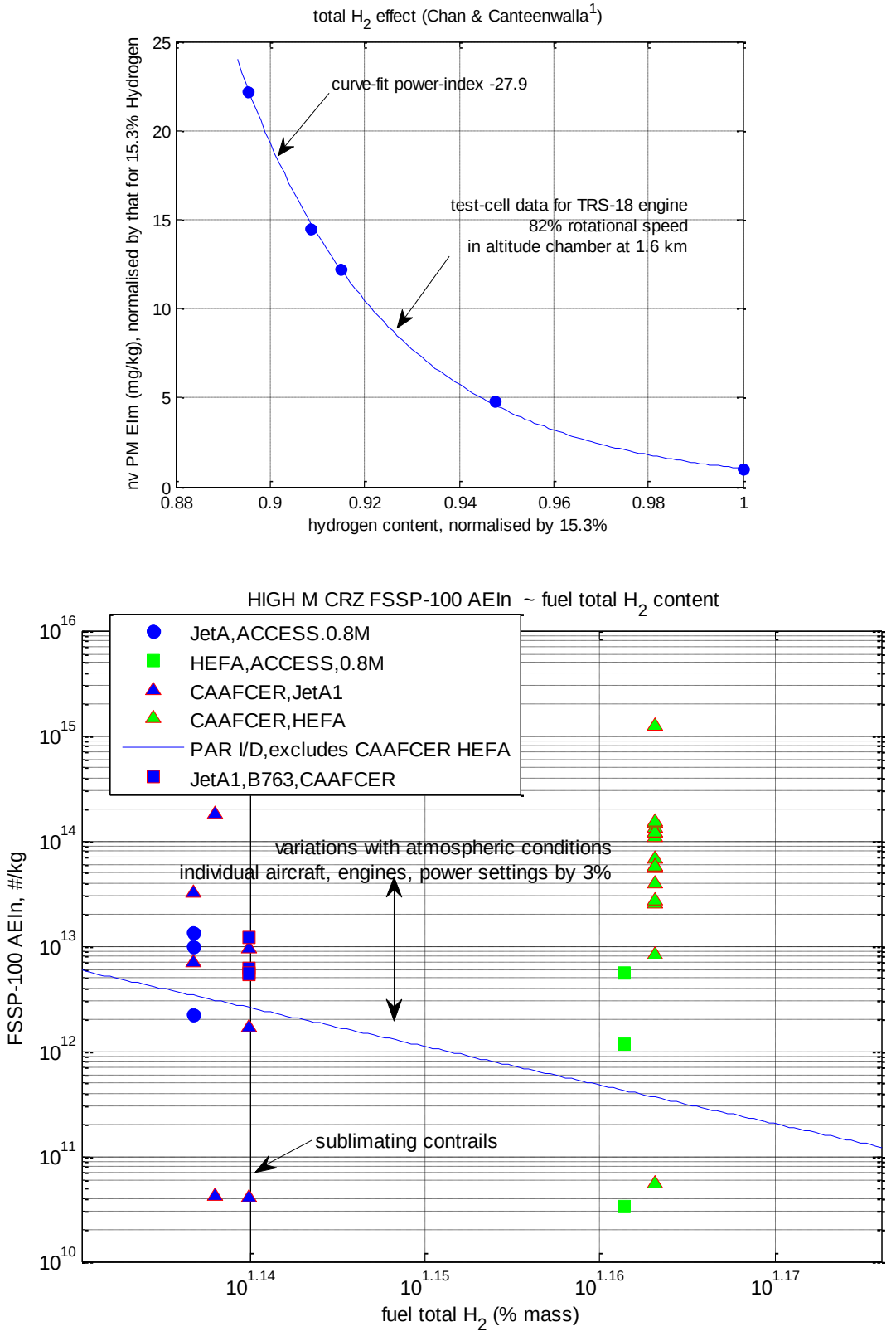

Figure 8 – (*top*) plot of nvPM EIm against total hydrogen content (normalised by 15.3%) for five jet fuels tested in the altitude chamber of the Gas Turbine Lab of the NRC [8]; curve-fit is the variation nvPM EIm ~ (total hydrogen)-27.9; ((*bottom*) plot of contrail FSSP-100 AEIn against total hydrogen content; ordinate direction spread includes the effect of variations in atmospheric conditions, such as RH_{iice}, individual aircraft, engines, power settings±3%; the log-log linearization shown is for CAAFCER JetA1 and ACCESS II Jet A and HEFA-blend., resulting in a power index of -36 [4].

Classification: Unclass
Distribution: Unlimited

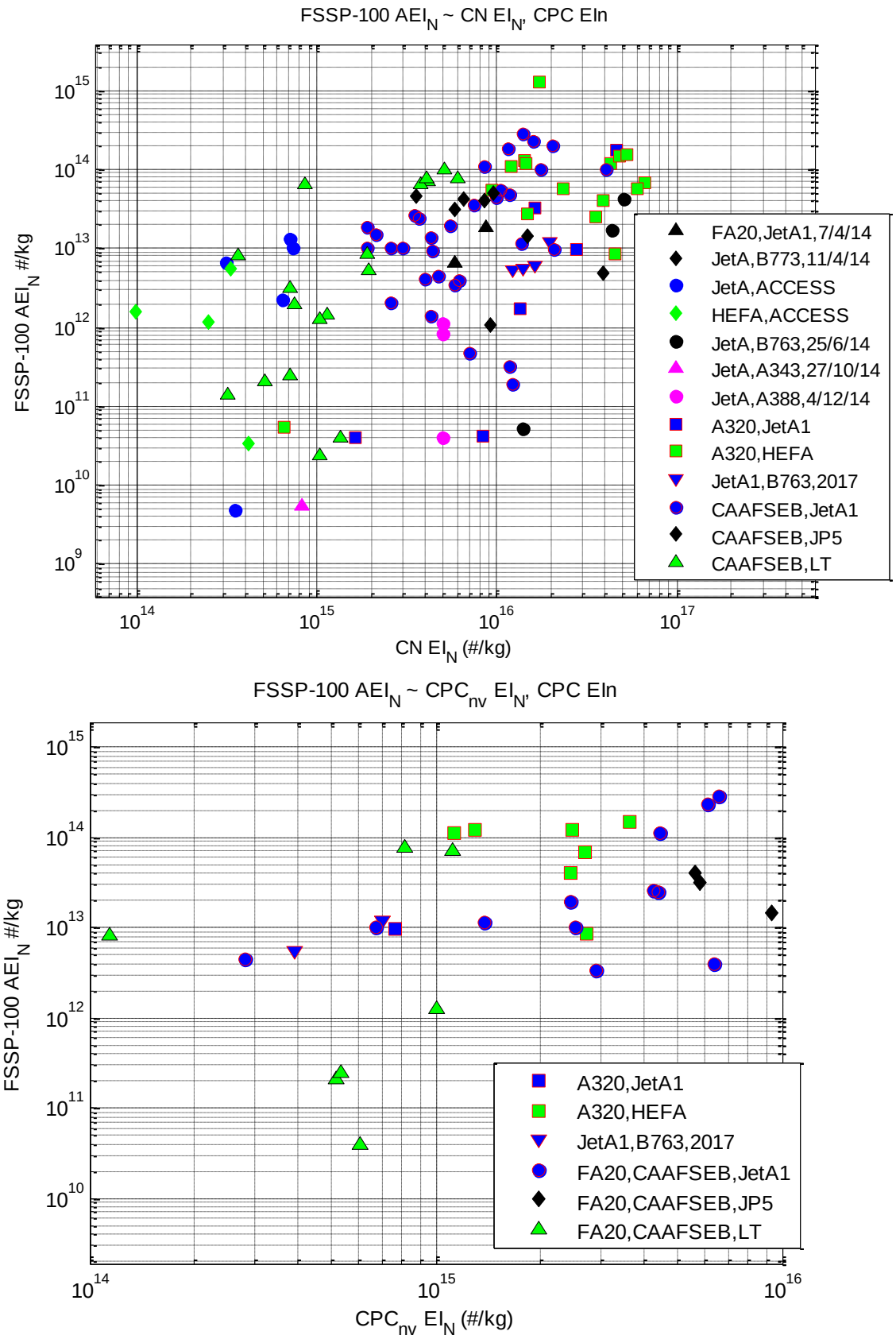

Figure 9 – assemblage plots of *all* NRC contrail FSSP AEIn data holistically-measured by the NRC CT-133, plotted against simultaneously-measured *(top)* CN EIn, and *(bottom)*, CPCnv EIn for a variety of Heavy Category and Medium Category jet transport aircraft [2][4].

Classification: Unclass
Distribution: Unlimited

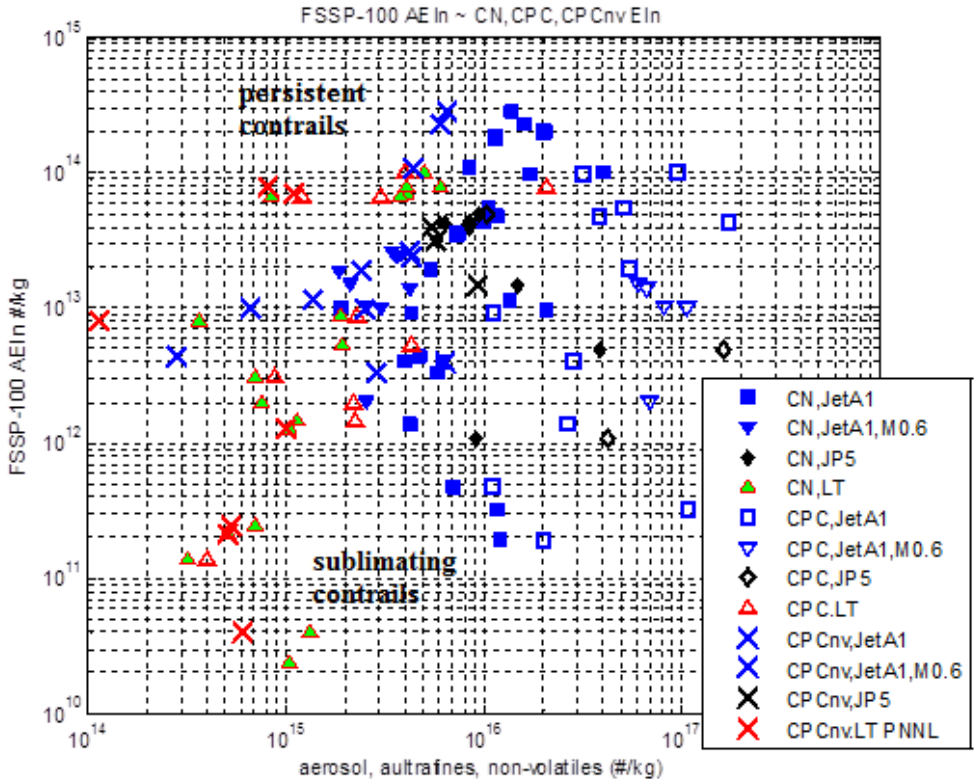

Figure 10 – assemblage plot of *all* CAAFCEB contrail AEIn values, for the FSSP-100 cross-plotted against CN, CPC & CPCnv values, for each of the three fuel types. NOTE: CPC 3776 used sheath flow to count ultrafine aerosol, errors at high altitude would be ±40%; CN errors approximately ±20% and FSSP errors approximately ±10%.

4.4.4 In comparison to the petroleum fuels, for the 92% LT PNNL / 150ND fuel blend, the margin between CN and CPC EIn was much lower indicative of comparatively less particles in the size range 2.5-10 nano-m. In part, these differences were attributable to sulphur (the LT PNNL/150ND had essentially no sulphur content); also possibly attributable to the hydrocarbon molecular composition. In particular, the JP-5 has higher carbon and lower sulphur compared to Jet A1 – these effects appear to offset each other, insofar as CN and CPC EIn mean values (extracted from Figure 10 and placed into Table 3) were essentially the same for JP-5 and JetA1. This is reasonably consistent with data, notwithstanding measurement uncertainty and some likely differences between young contrails at M0.6 and M0.8, because mean-overall CPCnv (probably, mostly soot) EIn was higher for JP-5 than for Jet A1, 6.8873/3.4705=1.98, *i.e.*, a 98% increase. This is a similar comparative value to the soot mass EIm change that would be expected from Figure 8, based upon the ground test cell data relationship of Chan *et al* [8], wherefore, for the mean hydrogen content values of Table 2, an increase of 96% was expected, $(13.52/13.85)^{-28} = 1.96$. Notwithstanding the ±40% absolute reading error of the sheath-flow CPC counter, given that the error could reasonably be expected to be relatively similar magnitude and direction, in similar cruise atmospheric environments, this observation potentially points to greater production of emitted soot particles at high altitude for the high-carbon petroleum fuel.

4.4.5 The comparison in EIn for CPCnv, between 92%LT PNNL / 8%150ND and JetA1, a ratio of 0.194 (Table 4), scaled to hydrogen content at an index of 22.2, *i.e.* $(13.74/15.33)^{22.2} = 0.194$. Engine test cell BC EIm ([8] and Figure 8), scaled to hydrogen content with an index of 28.

Classification: Unclass
Distribution: Unlimited

Table 4, CAAFCEB mean values of EIn for aerosols, ultra-fines, non-volatiles

Fuel	Mean values of EIn for			
	CN	CPC	CPCnv	CPCnv/CPC
JetA1	1.1286e+16	4.6236e+16	3.4705e+15	0.0751
JP5	1.3311e+16	5.6662e+16	6.8873e+15	0.1216
LT PNNL	1.9884e+15	4.1636e+15	6.7268e+14	0.1616
Ratio to JetA1	0.1762	0.0901	0.1938	

4.4.6 As a potentially worthwhile observation, given (a) the presence of sublimating contrail AEIn data points in Figure 10, and (b) margins between volatile and non-volatile ultra-fines for petroleum fuels and for LT PNNL biofuel, there is thus observed to be no strong association between AEIn and CN, CPC or CPCnv EIn – this observation would imply that particle shattering or disintegration was not a significant occurrence in the measurements. The differences in JetA1 and 92%LT PNNL/8%150ND particulate emissions can be observed in the dramatic differences in CN and CPC measurement time-traces during the JetA1 to LT PNNL to JetA1 transitions, as shown in Figure 11.

4.5 Contrail persistence

4.5.1 The path to persistence is indicated in Figure 12, including a linear-time plot for young contrails (<5 minutes age, *left* plot) and a log-time plot (*right* plot, highlighting the comparatively aged contrail state) of FSSP AEIn against contrail age for all contrail re-constructions. It is seen that AEIn stabilised at reasonably constant values by ages of 0.4 minutes (JP-5), 0.8 minutes (LT PNNL) and 1.5 minutes (Jet A1) for various contrails (not necessarily a function of fuel type). Furthermore, the 'nose-dive' to sublimation for the JP-5 contrail, at 1.7 minutes age, was indicative of relatively homogenous background atmospheric conditions from age = 0.3 to 1.7 minutes, equating to a contrail length from 4 to 26 km, which took 5.75 minutes for the CT-133 to survey, at M0.6, an air distance of 65 km, a typical lateral extent of homogenous atmospheric conditions in the CAAFCEB flights.

4.5.2 It is seen in Figure 12 that there were several instances of relatively spatially-sharp sublimation (evidenced by marked reductions in AEIn), followed by recovery of AEIn. There patches were evidence of pools of lower RH in the background atmosphere. In a similar process to the previous paragraph the scales of such pools have been converted to air-mass spatial scales in the range of 40-60 km. The log-log scale of Figure 12 (*right*) highlights the sublimation (loss of AEIn) that accompanied one such dry pool in the air-mass presence of the relatively-aged contrail, amidst the stabilised thin cirrostratus that the contrail had transformed to, on either side of the dry pool (higher AEIn on either side, by a magnitude difference >1 log-decade).

4.5.3 Figure 12 also implies low production of ice particles in contrail formation for LT PNNL *c.f.* Jet A1 fuels – an order of magnitude lower for age < 0.5 minutes, and a ¼ to ½

Classification: Unclass
Distribution: Unlimited

order of magnitude lower for constant AEIn with age > 2 minutes. However, this is dependent upon differing background atmospheric conditions, discussed in the next section.

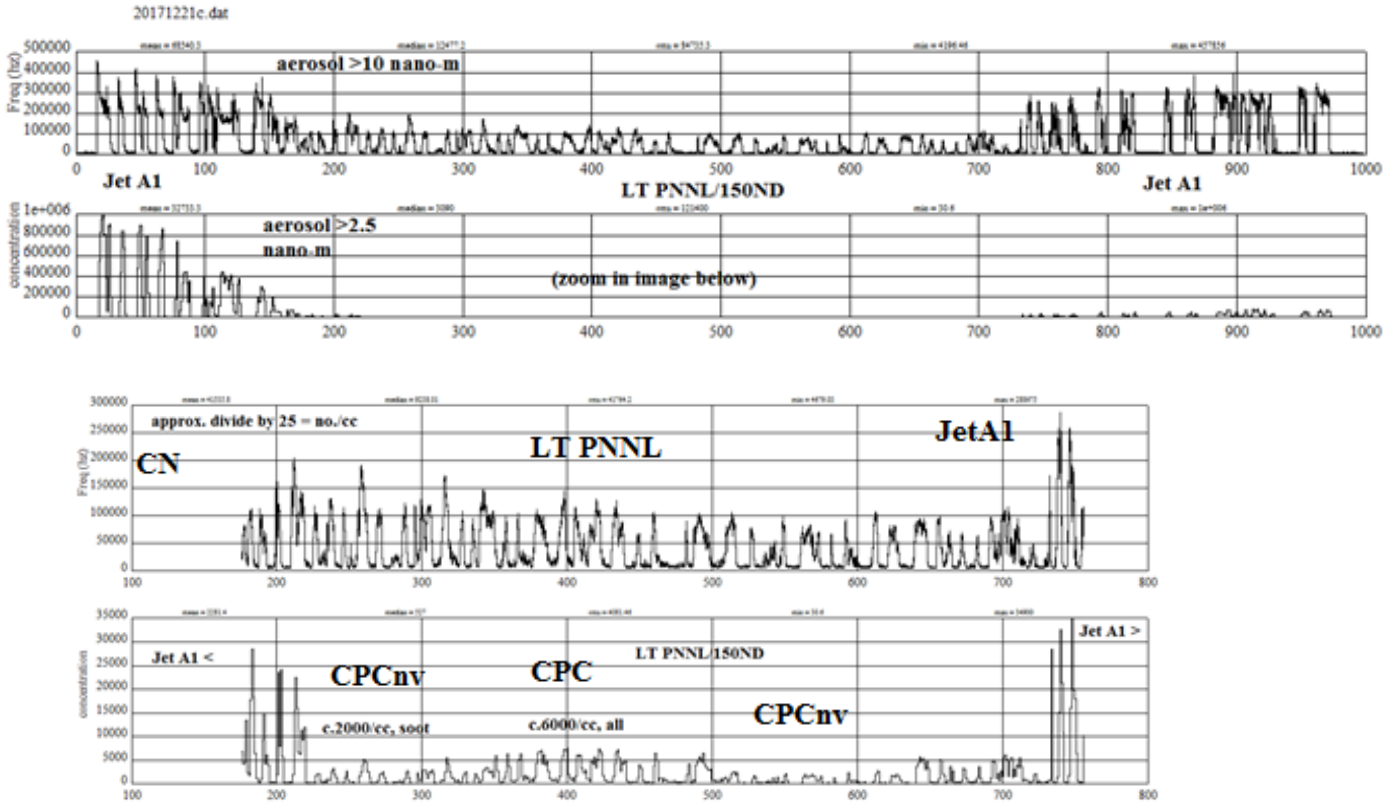

Figure 11 – time-traces of CN (*top*) and CPC, CPCnv (sequentially) (*bottom*), during JetA1 then LT PNNL then JetA1 transitions.

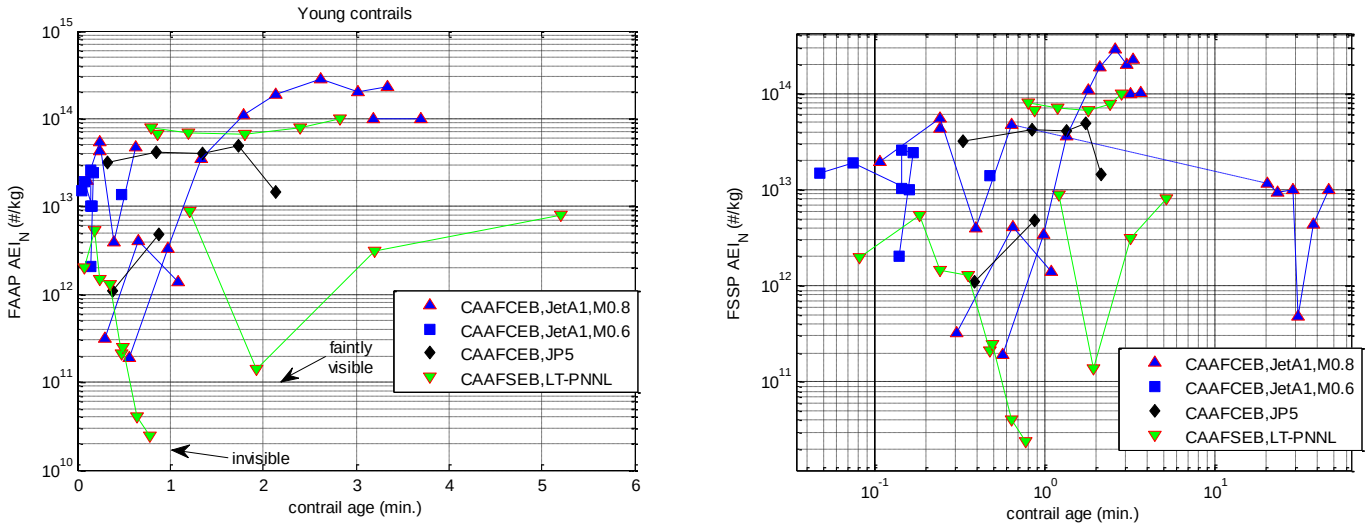

Figure 12 – plots of CAAFCEB contrail AEIn values against contrail age for (*left*) contrails <5 minutes age and (*right*) all contrails, highlighting the comparatively aged contrail segment.

Classification: Unclass
Distribution: Unlimited

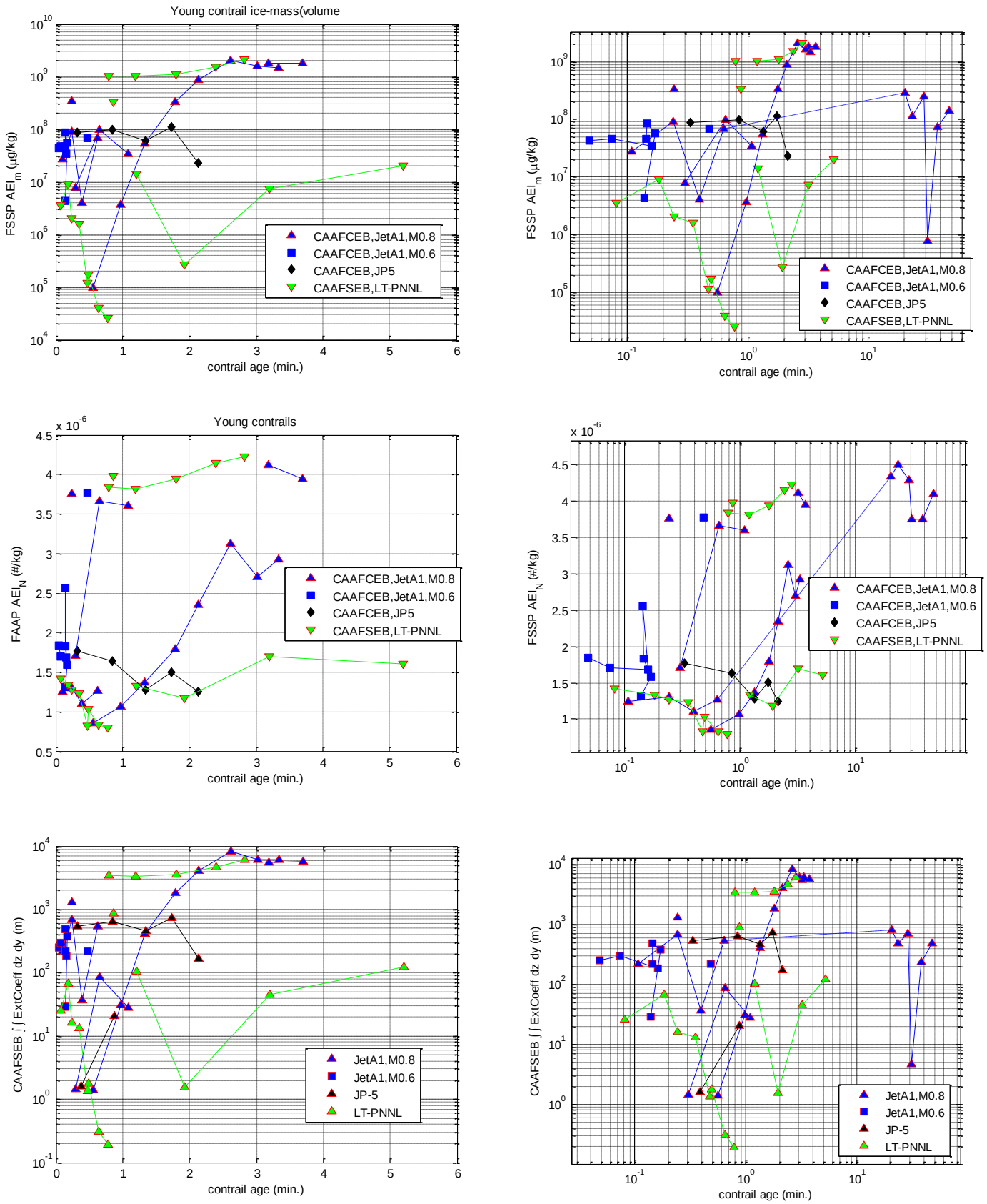

Figure 13 – plots of CAAFCEB contrail AEIm (*top*), medMED (*middle*) and AECzy (*bottom*) values against contrail age for (*left*) contrails <5 minutes age and (*right*) all contrails.

Classification: Unclass
Distribution: Unlimited

4.5.4 Other contrail cross-sectional parameters can be plotted similarly, against contrail age. This has been done in Figure 13, for each of (i) AEIm, (ii) *medMED*, defined as the median value of each re-constructed cross-sectional distribution of contrail ice particle MED, and (iii) AEC_{ZY} (discussed in the next section). Of these parameters, AEIm and AEC_{ZY} roughly followed the contrail age characteristics of AEIn, in response to changing atmospheric conditions, in particular states of sublimation, growth or stabilisation. medMED, on the other hand, appeared to not have been as responsive – for the aged contrail segment (Figure 13, *right*), the dry pool reduced AEIm and AEC_{ZY} >2 orders of magnitude, whereas medMED dropped from 4.5 μm to 3.7 μm before recovering.

4.5.5 As observed in Figures 12 and 13, sublimation rates in dry pools, when they occurred, were similar between contrails; likewise for growth rates, which generally appeared to be very high, more than two orders of magnitude in AEIn (for ice particle >0.5 μm in size) per minute. The translational effect of flying across more moist pools of background RH (or less moist), discussed previously, is one factor associated with this – in other words it was a spatial effect, evidence of relatively high lateral spatial gradients of RH, at entry to and exit from the dry pools.

4.5.6 Statistical sizes and growth rates, as depicted by the contrail cross-sectional medMED parameter, displayed in Figure 13, an apparent bifurcation in size state between many at 1-1.5 μm and 3.5-4.5 μm. The 30-45 minute contrail displayed the largest medMED value, 4.5 μm, which was still a relatively small value. Nevertheless, AEIn was still maintained relatively high, within a decade of the peak values for the young contrail. However, given the transformation to Cs on this occasion and the lateral spread, it is speculated that these type of contrail transformations could possibly be the most significant from a RF perspective.

4.5.7 High ice particle sizes do occur in contrails, as evidenced visually by the gravity fall-out of ice from some contrails, in the form of 'mare-tails' generally the centerlines of the contrails. The consequence of fall-out is inevitable evaporation of the ice particles at lower altitudes, thereby ending the contrail.

4.6 Contrail optical properties

4.6.1 The contribution of contrails to global warming is through the process of radiative forcing in response to incident solar radiation. Contrail radiative forcing properties relate to the energy balance between reflected, transmitted, scattered and absorbed solar radiation. Significant parameters affecting this balance are radiative-effective ice particle size, shape, number and the extinction coefficient induced by the ice particles.

4.6.2 Effective size (D_{eff}) and Extinction Coefficients (EC) for the FSSP-100 spectra have been derived using the methodology of Korolev, Shashkov and Barker [6], with an inherent assumption of sphericity. A cross-sectional contour plot of EC was presented in Figure 5. It is seen that peak EC values were high (maxima values, 10-11 km^{-1}), indicative of dense opacity of the contrail. However, as with other properties, there was a wide range of EC values in every re-constructed contrail cross-section. Integration of EC with contrail extent, in a direction relevant to the solar angle, provided a measure of optical depth (OD, non-dimensional). In the present work, only the zenith direction was considered.

4.6.3 As shown in Figure 5, OD was inevitably non-homogeneous, not only at the edges, but also across the centre of the cross-section. Therefore, in the present work, second

Classification: Unclass
Distribution: Unlimited

integrations across the lateral extent of the contrail cross-sections were conducted, termed AECzy, as an apparent emission index of integrated optical effect (of FSSP-100 sensed spectra), i.e. $AECzy = \iint ECdzdy/(TAS/FF)$, mkg^{-1} of fuel – the quantity represented the sum optical effect of the contrail (in a defined solar direction, in this case zenith) as an apparent emission index.

4.6.4 The behaviour of AEC_{ZY} with contrail age is displayed in Figure 13. Values varied between 0.2 m/kg for essentially invisible contrails, to 10-100 m/kg for persistent light contrails, to 1,000-10,000 m/kg for persistent, thicker contrails. The maximum values occurred for JetA1.

4.7 Contrail AEIn atmospheric parameterisations

4.7.1 Analysis of NRC contrail data from NASA ACCESS II [1][2] indicated that the atmospheric property vector [T_S RH_{ICE} $\partial RH/\partial z$] was consequential for variations in AEIn, *i.e.* microphysical processes involved in the downstream deposition and/or sublimation of ice particles, was significantly affected by this parametric vector.

4.7.2 Of these parameters, the RH lapse rate, $\partial RH/\partial z$, was noteworthy, because the DC-8 contrails were non-UJW type; rather they were almost entirely TWV contrails. The DC-8 trailing vortices contained vortex core expansions (increasing RH_{ICE} in the cores) and mutually-induced downwards descent velocities of approximately 2 m/s. RH lapse rates varied along the DC-8 contrails, and this was observed in AEIn values.

4.7.3 The NASA DC-8 contrails were sublimating, whereas the Air Canada A320 (project CAAFCER) and NRC FA20 (present high-blend project CAAFCEB) contrails in the Val d'Or- Montreal-Ottawa-Toronto region that were persistent UJW-type, were observed and measured to be amidst background atmospheric positive lapse rates [2,4].

4.7.4 This parameter has been retained for the present analysis, in favour over another lapse rate variable. In particular, Richardson Number, Ri, has been considered in this regard, essentially a ratio of buoyancy to shear for the background atmospheric conditions. However, contrails are formed in the wake regions of aircraft, under the extremely energetic action of trailing vortex formation and dissipation (itself, a long process, which can easily take five minutes and 2,000 feet of downwards displacement). EDR or TKE values in the wake region correspond to those of the most extreme atmospheric turbulence, and thus completely nullify any background atmospheric turbulence. Thus, Ri would need to be based upon wake turbulence and therefore would always be low in value, thereby lacking discrimination of background atmospheric conditions. Thus, it has not been applied to CAAFCEB analysis, wherefore persistence in contrail formation was determined in the first minutes of young contrail life. The primary dependency is expected to be RH_{ICE}.

4.7.5 Plots of AEIn ~ [T_S RH_{ICE} $\partial RH/\partial z$] for young contrails, are shown in Figure 14, including the NRC data from ACCESS II and CAAFCER (both of which have been normalised for hydrogen and sulphur content). Also presented are model output data from Karcher, [10], for an EI_S value of 10^{15}/kg. The apparent rise in AEIn with reducing T_S, obtained inflight, is also indicated in the Karcher model data [10], *albeit* with a maximum AEIn at a higher T_S value than the model, approximately -51°C *c.f.* -57°C, respectively.

Classification: Unclass
Distribution: Unlimited

4.7.6 The scatter in the AEIn~∂RH/∂z plot is large, whilst the relationship against RH_{ICE} is quite regular, as expected.

4.7.7 As shown in Figure 14, functional relationships have been assigned to enveloping data-fits in these curves. Having assigned functional relationships for the individual effects upon contrail FSSP AEIn of the atmospheric parameters of T_S, RH_{ice} and ∂RH/∂z, the following product-power-law relationship was used as an empirical correlation function. In the past, such expressions have frequently been employed in non-adiabatic fluid-flow and the convective heat transfer associated therewith, *e.g.*, Stanton, Prandtl and Nussult Numbers.

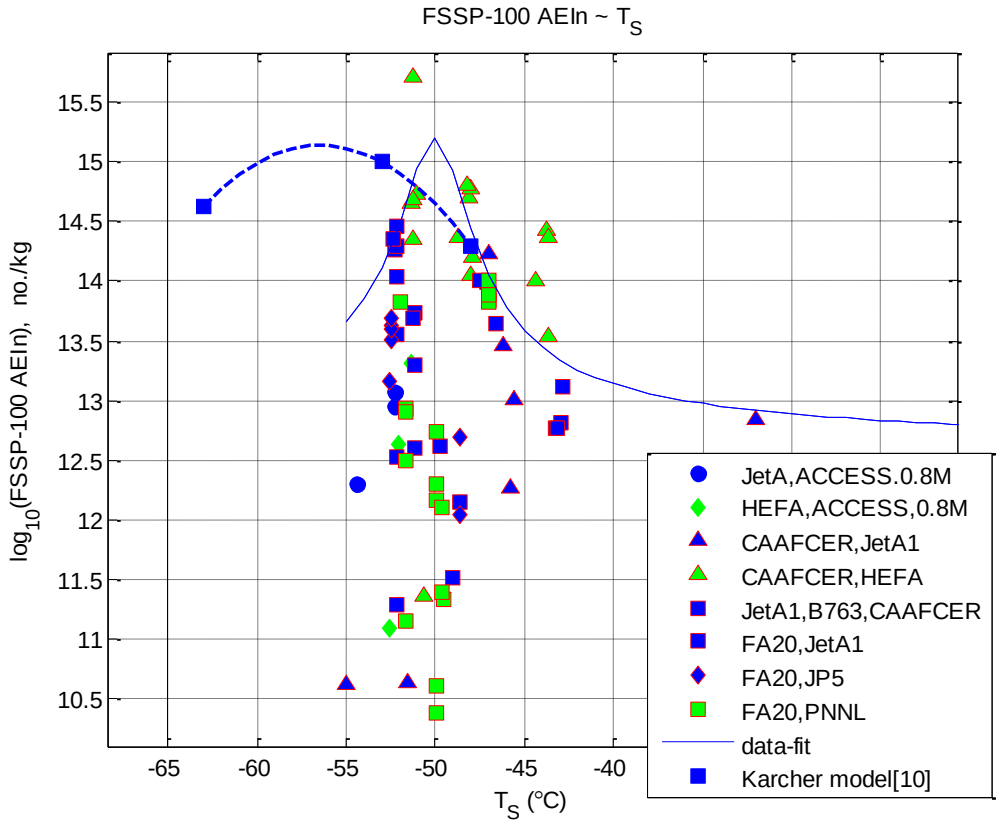

(a) (Figure continued with caption, overpahe)

Classification: Unclass
Distribution: Unlimited

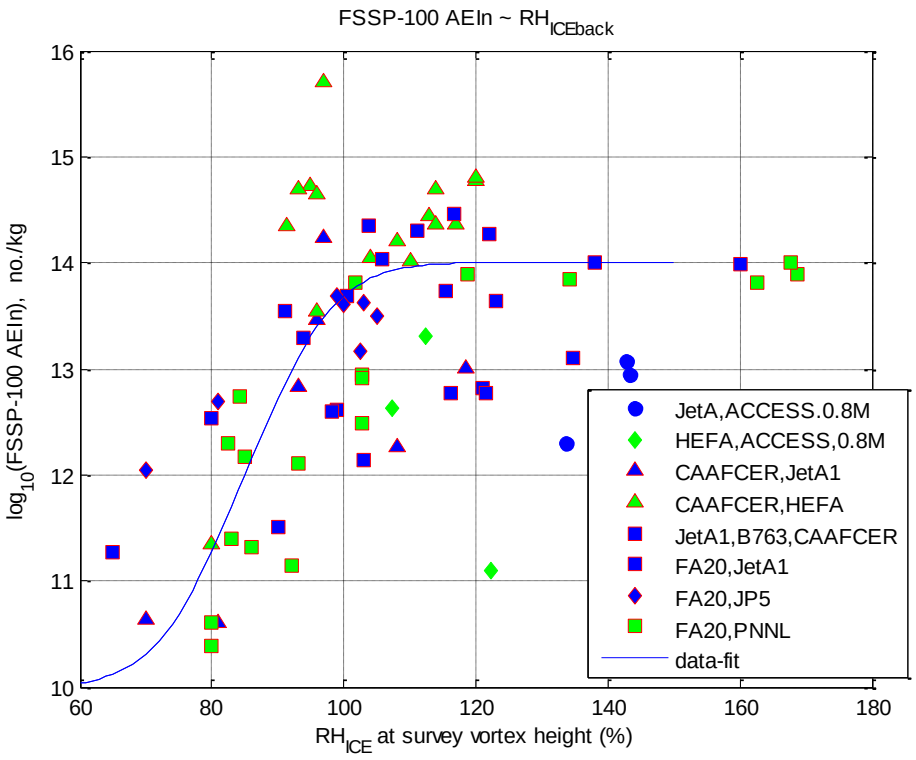

(b)

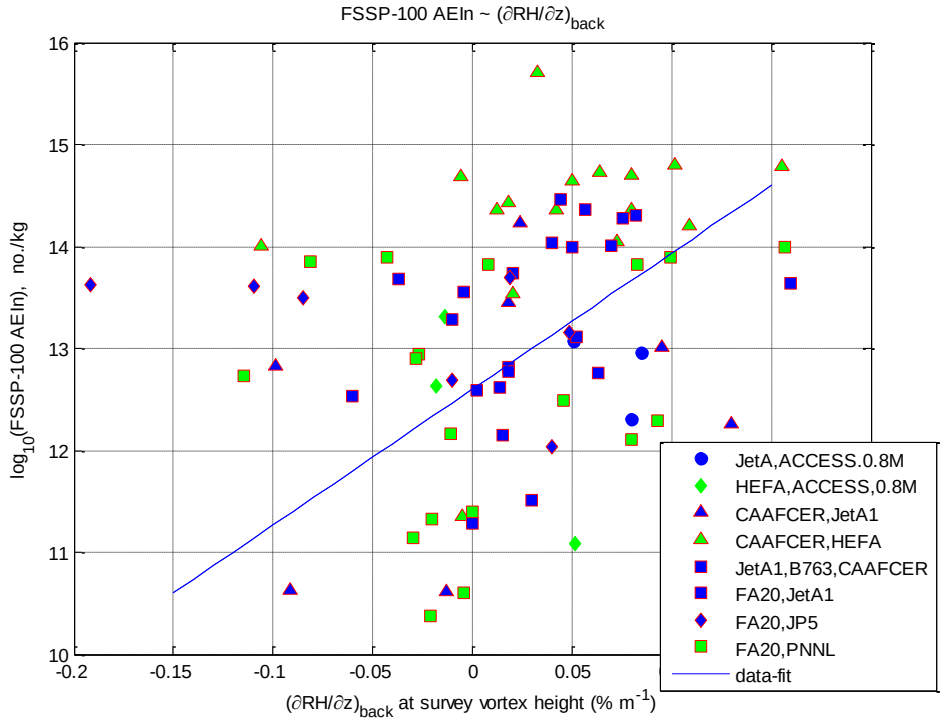

Figure 14 – plots of NRC data from ACCESS II, CAAFCER and CAAFCEB contrail AEIn values against (a) T_S, (b) RH_{ICE}, and (c) $\partial RH/\partial z$.

Classification: Unclass
Distribution: Unlimited

4.7.8 For CAAFCEB contrails, the following has been used,

Log_{10}[FSSP AEIn, *for each of JetA1 & LT PNNL*] = $A(\partial RH/\partial z)^a T_S^b RH_{ice}^c$

For solution (*i.e.*, identification of the parameter vector [A a b c]), the expression was linearised by taking the additional logarithms of both sides. This results in a row vector of data-points (log(Log_{10}[FSSP AEIn])), and on the right side, the sum of atmospheric parametric row vectors. Thence, a Matlab® least squares vector identifier ('\' backslash or left-matrix divide operator) was used to identify the amplitude and exponent vector [A a b c], for each fuel type, Jet A1 and LT PNNL. In order to evenly weight the parametric influences, the assigned functional relationships were normalised, i.e. the vector [A a b c] identified for a unit value of (each log_{10}[FSSP AEIn] point) /typical(log_{10}[FSSP AEIn]). For this, log_{10}[FSSP AEIn]=15 was used. *Note:* for these identifications, A320 contrails (CAAFCER, with hydrogen and sulphur content, H&S, corrections incorporated) and current CAAFCEB contrails (no H&S corrections) have been used, with *separate* identifications for each aircraft and fuel type, in order to compare the empirical fits.

4.7.9 The results are shown in Figure 15. A320 data (project CAAFCER, [4]), *with* H&S corrections, were essentially the same AEIn, indicating that the fuel properties analyses discussed previously, was the principal effect in AEIn formation for different fuels. For present FA20 CAAFCEB data, it is seen that the AEIn for LT PNNL reduced *c.f.* Jet A1. This reduction amounted to a ratio of $10^{15*1.156}/10^{15*1.203}$ = 0.1972, close to the CPCnv mean value ratio between fuels 92%LT PNNL/8%150ND and JetA1, discussed earlier. In other words, the LT PNNL contrails had an 80% reduction in ice particle AEIn, which was in proportion to the reduction in soot number, EI_S. This result was in accordance with the soot-effect modelling of Karcher [10], for which the reduction was log-linear in the soot-rich regime, *i.e.* $EI_S > 10^{14}$.

4.7.10 As a comparison *without* parameterized corrections for variations in atmospheric properties, the mean values for sub-sets of stable young contrail (*i.e.*, leading to persistence) cross-sections for RHice$\geq$100%, for which mean AEIn for LT PNNL = 5.3146e+13; for JetA1, 1.1387e+14, with the atmospheric variations as shown below in Table 5. Thus, the AEIn ratio for LT-PNNL to JetA1was 0.46, more than the $A(\partial RH/\partial z)^a T_S^b RH_{ice}^c$ ratio, above, and the CPCnv ratio for the fuels, both of which were approximately 0.2.

4.7.11 Experimental error and other considerations to be mindful of include (i) the sensitivity of the product-power-law identification to invisible contrails, possibly the least accurate AEIn, (ii) the CPC 3776 instrument error of $\pm$ 40% at low pressure (the CPCnv trends however appear accurate, when assessed against total hydrogen estimates), (iii) the effects of impure aerosols, including potential VOC aerosol effects, upon ice nucleation, and (iv) the effects of impure sulphate aerosols upon ice nucleation ([4] data implied a direct AEIn correlation with sulphur of the order of ¼ that of ultrafine aerosols with sulphur, [9]).

Classification: Unclass
Distribution: Unlimited

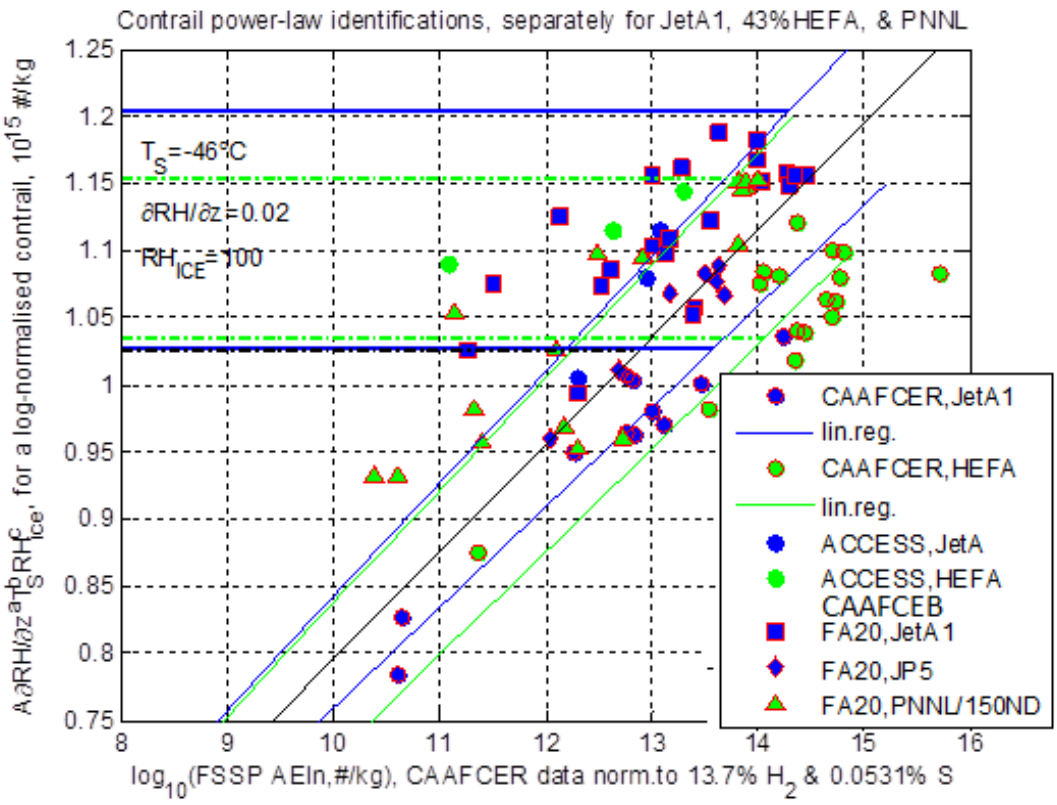

Figure 15 – plots of $A\partial RH/\partial z^a T_S^b RH_{ice}^c = \log_{10}$[FSSP AEIn], identifications for *each* of the CAAFCEB fuels, Jet A1 (blue) and LT PNNL (green). Also presented are the different identifications for the Jet A1 and the 43%HEFA-blend used ona Air Canada A320 CAAFCER project.

4.7.12 Also for 92%LT PNNL/8%150ND *c.f.* JetA1, as seen in Table 5, when uncorrected for the differences in atmospheric properties between fuels' RHice_>_100% subsets, CPCnv was 85% lower (implying, AEIm was 10% lower, median MED, 8% larger, and AECzy 27% lower. Concerning the differences between atmospheric properties, the mean RHice (≥100%) were 129 for LT PNNL and 117 for JetA1, which would lessen the different effects between fuels. Thus, it can be concluded for LT PNNL contrail optical properties, that AECzy would be >27% lower than for JetA1.

Table 5, CAAFCEB young contrails at M0.8: mean values of non-volatile ultrafine aerosols >2.5 nano-m (≈EIs), atmospheric and contrail properties for the RHice ≥ 100% sub-sets of data.

Fuel	Mean values of atmospheric properties			CPCnv x 10^{15}	Mean values of contrail cross-sectional properties, without corrections for atmospheric differences			
	T_S (°C)	RHice	∂RH/∂z (%/m)	instr. Error ±40%	AEIn (#/kg) x10^{14}	AEIm (µg/kg) x10^{8}	Median MED (µm)	AECzy km/kg
JetA1	-50.4	117	0.048	4.4375	1.1387	8.88	2.93	3.42
'A-3' JP-5	-52.4	103	-0.084	6.8873	1.0164	6.73	1.48	4.55
92%LT PNNL 8% 150ND	-49.1	129	0.024	0.6821	0.5315	7.91	3.17	2.49

Classification: Unclass
Distribution: Unlimited

4.7.13 The measured, fuel-comparative contrail properties of Table 5 were likely influenced by the relatively small sub-set (there were two flights on 'A-3' JP5, six JetA1 flights and four LT PNNL flights) and, in particular, the low mean value of RHice ($\underline{\geq}$ 100%) of 103% and negative RH lapse rate. Thus, it could be concluded for 'A-3' JP-5 that the AECzy would be >33% larger than for JetA1, in similarly favourable atmospheric conditions.

4.7.14 Contrail ice-mass, assuming sphericity and ρ=1000 kg/m^3 (most likely density would be less due to entrapped air), has been empirically treated, likewise (Figure 16). It is seen that greater scatter was prevalent for LT PNNL in particular. For JetA1, the solution did not converge with the inclusion of the final flight data (which was drawn from a different NRC fuel-farm tank). Finally, hinging of the solutions at very low ice-mass, where the solutions for the different fuels merged together, was necessary for LT PNNL solution convergence. Possibly the most significant reason for the empirical convergence difficulty was the assumption of ice particle sphericity. Thus, this empirical fit process was not particularly reliable. Sensibly, the values from Figure 16 for the reference atmospheric conditions, were the same for the two fuels, because the difference was well within the scatter; specifically the LT PNNL appeared to have marginally less spherical ice-mass, *c.f.* Jet A1, in the ratio of $10^{8*0.9564}/10^{8*0.9688} = 0.80$, implying a 20% reduction in ice-mass for LT PNNL. Confirmation was required from another source, as provided below.

4.7.15 In a similar manner to AEIn, the change in AEIm between fuels could also be estimated by considering the AEIm sub-sets for RHice $\underline{\geq}$ 100%. The AEIm characteristics against T_S and RHice are presented in Figure 17. The mean values for the sub-sets were 1.151e+09 and 0.791e+09 µg/kg for JetA1 and LT PNNL, respectively. Thus, for RHice $\underline{\geq}$ 100%, the ratio of AEIm for LT PNNL *c.f.* JetA1, was 0.69 (*i.e.*, a 31% reduction for LT PNNL), *c.f.* the empirical fit identification ratio value of 0.80.

4.7.16 Assuming sphericity, a ratio of mean ice particle size can be estimated as $((AEIm_{-LT}/AEIm_{-JetA1})/ (AEIn_{-LT}/AEIn_{-JetA1}))^{1/3} \approx (0.69/0.20)^{1/3} = 1.5$, or a 50% increase for the reference atmospheric conditions of [-46°C 100% 0.02 %/m]. This can also be checked against the contrail cross-sectional median MED ice particle size sub-sets for RHice $\underline{\geq}$ 100%. The mean values were 2.91 µm for JetA1 and 3.17 µm for LT PNNL (at the mean values of flight conditions, colder than the reference atmospheric temperature for example), a 9% increase in median MED for the latter.

4.7.17 In comparison, the model analysis of Karcher [10] had an outcome of constant ice particle size with reducing EI_S, at the flight T_S and flight EI_S values.

4.7.18 Figure 18 shows the behaviour of contrail cross-sectional median MED values with T_S and RHice. The behaviour is seen to have been considerably more complex than that of AEIn and AEIm relations with T_S and RHice (Figures 14 and 17, respectively). One A320 and all B763 medMED values were in the range of 7 µm, approximately twice the FA20 sizes. Whether in relation to T_S or RHice, the FA20 medMED values appear to have demonstrated bi-modal characteristics (bifurcating into more than one characteristic line).

Classification: Unclass
Distribution: Unlimited

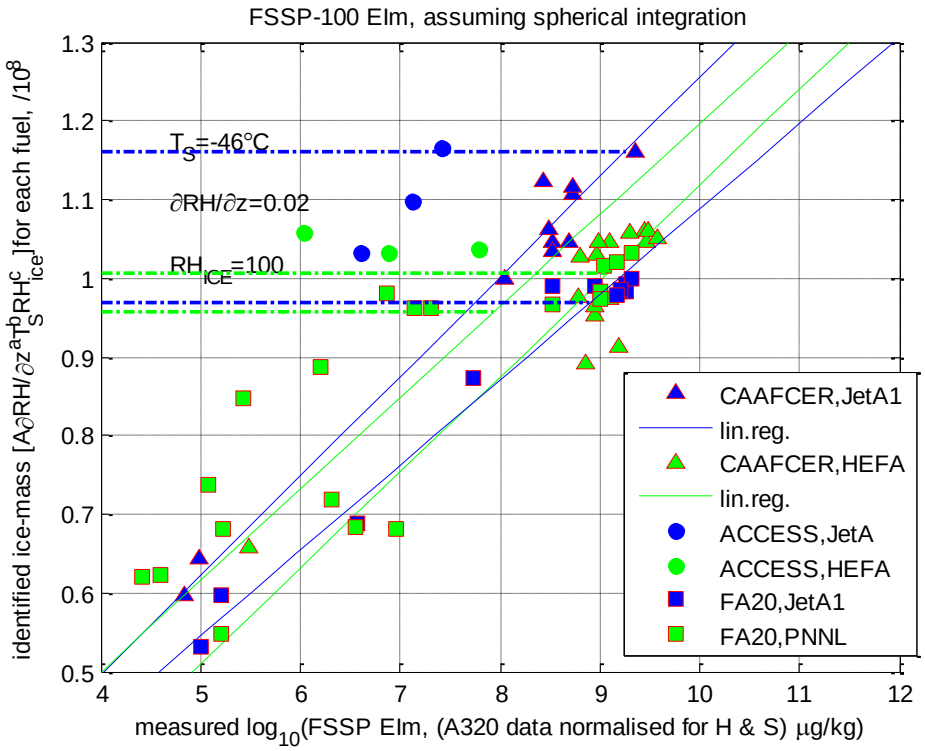

Figure 16 – plots of $A\partial RH/\partial z^a T_S^b RH_{ice}^c = \log_{10}$[FSSP AEIm], identifications for *each* of the the CAAFCEB fuels, Jet A1 (blue) and LT PNNL (green). Also presented are the different identifications for the Jet A1 and the 43%HEFA-blend used on an Air Canada A320 CAAFCER project.

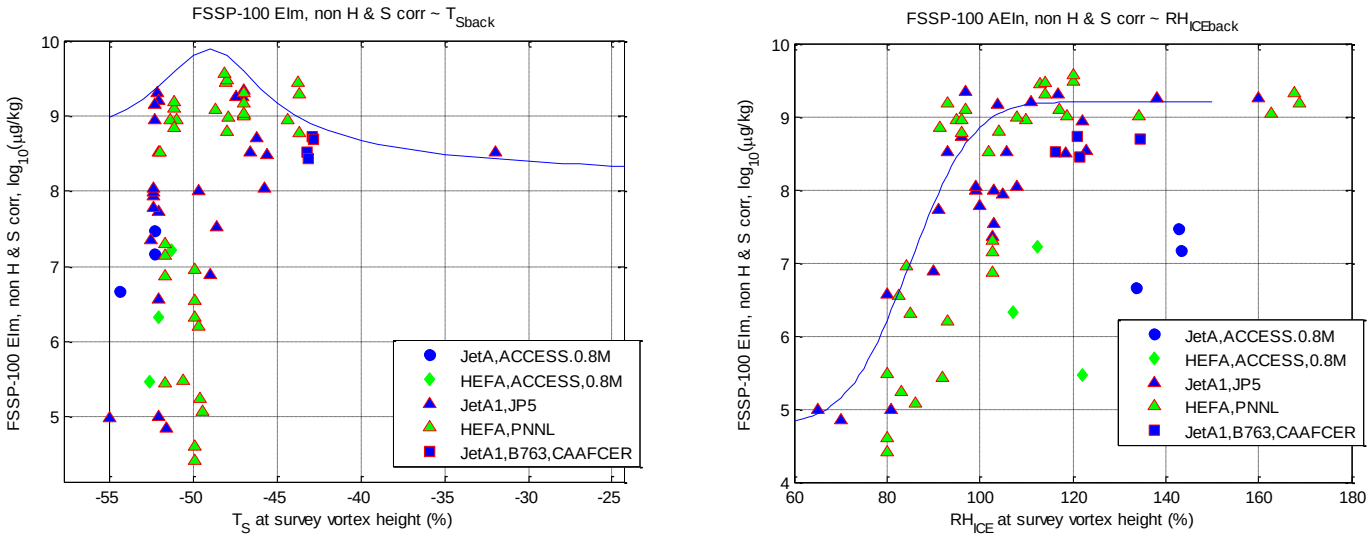

Figure 17 – variations of AEIm with T_S and RHice, for lumped CAAFCEB and CAAFCER data-sets of petroleum fuels, biofuels (HEFA, PNNL) and ACCESS II fuels.

Classification: Unclass
Distribution: Unlimited

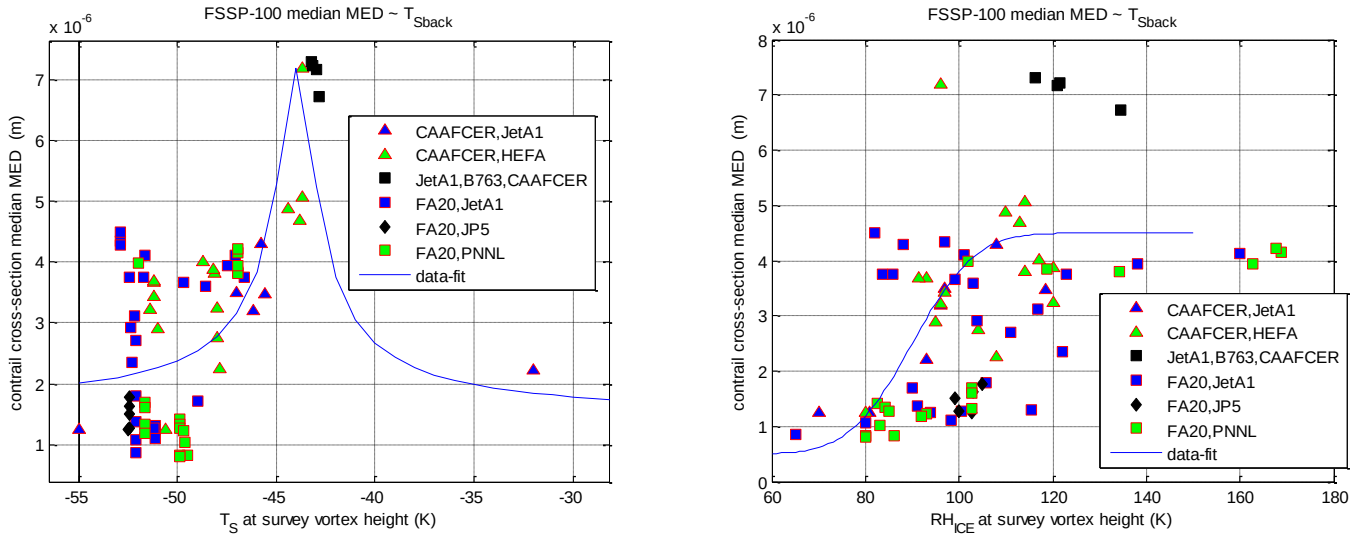

Figure 18 – relationship between contrail cross-sectional median MED and (*left*) T_S and (*right*) RHice.

4.8 Contrail optical properties atmospheric parameterisation

4.8.1 Earlier in the report, the concept of an Apparent Extinction Coefficient emission index was introduced (section 4.6). Magnitudes and trends with contrail age were presented (Figure 13). $A(\partial RH/\partial z)^a T_S^b RH_{ice}^c$ parameterisation for variations in atmospheric parameters, [T_S RHice $\partial RH/\partial z$] as before, can be conducted for AECzy, similarly to the other apparent contrail properties AEIn and AEIm. The variations of AECzy with atmospheric parameters are shown in Figure 19.

4.8.2 This identification was robust. Significantly, orders of magnitude reductions in AECzy with reducing RHice dominated the behaviour of AECzy, with the reductions being regular and monotonically progressive for very thin and invisible contrails (AECzy < 1 m/kg approximately). The enveloping of the $\partial RH/\partial z$ effect upon AECzy (a positive slope) was more regular than AEIn or AEIm, whilst for RHice > 100%, AECzy increased with RHice until it plateaued above 120% RHice.

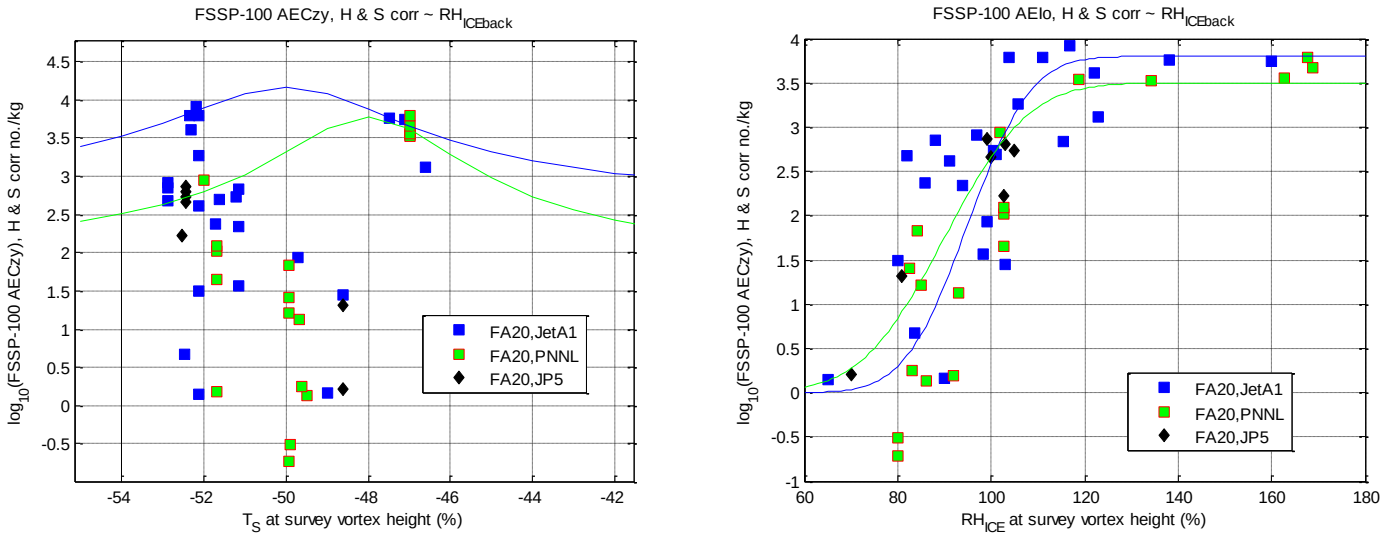

(Figure continued, with caption, over-page)

Classification: Unclass
Distribution: Unlimited

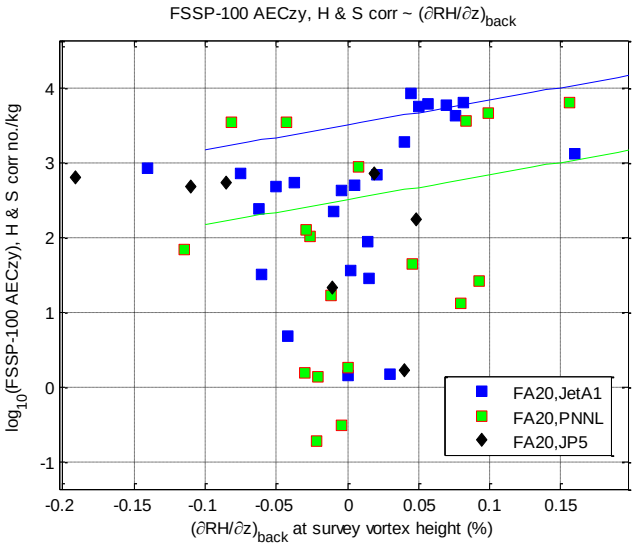

Figure 19 – plots of NRC CAAFCEB contrail AECzy contrail data against (a) T_S, (b) RH_{ICE}, and (c) $\partial RH/\partial z$.

4.8.3 The identified product-power-laws are presented in Figure 20. For the reference atmospheric conditions as before, the ratio between AECzy values for LT PNNL and JetA1, respectively, approximately ½, *i.e.*, a 50% reduction. On the other hand, as presented in Table 5, for the actual flight conditions (in particular, T_S ranging from -53 to -50°C) the RHice $\geq$ 100% data sub-sets yielded AECzy mean values of 2.5 km/kg and 3.4 km/kg for 92% LT PNNL/8% 150ND and JetA1 respectively, a ratio of 0.73. *i.e.*, 27% reduction in apparent extinction coefficient emission index for the LT PNNL fuel.

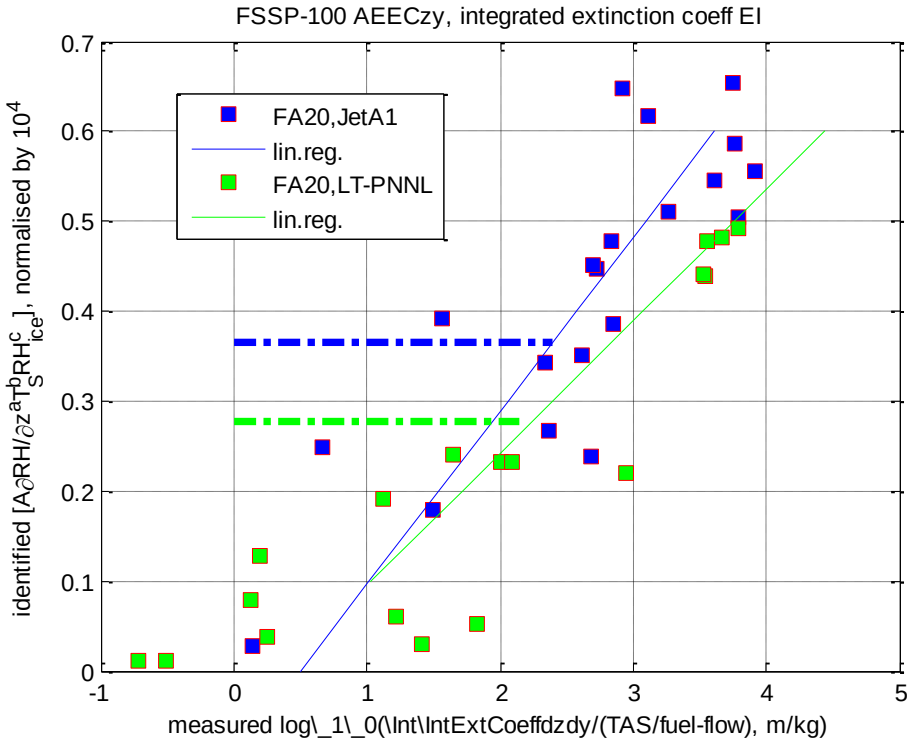

Figure 20 - $A(\partial RH/\partial z)^a T_S{}^b RH_{ice}{}^c$ parameterization of AECzy, the lateral integrand of optical depth per kg of fuel-flow (*i.e.*, as an apparent EI).

Classification: Unclass
Distribution: Unlimited

5. CONCLUSIONS

5.1.1 Persistent contrails are considered to give rise to atmospheric warming, through the process of radiative forcing. Project CAAFCEB has been conducted for flight research of the effects of biofuel on contrail formation. Four flights were conducted using, in 0.8M cruise, 92%LT PNNL LanzaTech ethanol-ATJ derived SPK biofuel, blended with 8% Solvesso 150ND mono-aromatics. An additional two flights were conducted burning 'A-3' JP-5 petroleum jet fuel in M0.8 high altitude cruise. For all flights, NRC fuel-farm JetA1 was used as the baseline fuel. The NRC Falcon 20 burned fuels, whilst the NRC CT-133 measured background atmospheric conditions, emissions and contrail characteristics.

5.1.2 The flights were conducted north of Ottawa, during winter, November 2017 to March 2018, inclusive. Contrail conditions with relatively-high atmospheric tropopauses were sought for each flight. The flight results indicated that water vapour aloft was non-homogeneous, 'pooling' into drier and moister regions of typical scale sizes 60-100 km.

5.1.3 Nevertheless a range of contrail conditions were obtained, ranging from intermittently sublimating-growing, generally sublimating, to consistent, lasting contrails. In the last category, on the last flight the CT-133 flew in-trail for JetA1, then head-on for LT PNNL, finally continuing in reverse-track and re-measuring the earlier JetA1 (after breaking-off, so that it was not contaminated by the emissions and contrail of the CT-133). In this manner, a JetA1 contrail was sampled at 45 minutes age, following transformation into thin, laterally-spread cirrostratus, which had an ice particle size and an Apparent EI of number similar to those of the contrail at formation.

5.1.4 The contrail data was analysed in re-constructed cross-sections, integrating and deriving (using TAS and fuel-flow) AEIn, AEIm (assuming sphericity) and AECzy (laterally-integrated optical depth, expressed as an AEI). Non-volatile ultrafine aerosol EIn behaviour for all fuels followed a total-hydrogen power-law relationship, somewhat less sensitively, though, than NRC/ECCC engine test cell data.

5.1.5 AEIn, AEIm and AECzy were successfully parameterised in a product-power-law (PPL) least-squares best-fit $A(\partial RH/\partial z)^{a}T_S^{b}RH_{ice}^{c}$, against atmospheric properties. The solutions were robust for AEIn and AECzy, but sensitive to the accurate measurement of invisible contrails for AEIm (possibly because of a necessary assumption of sphericity). The data sub-sets for $RH_{ICE} \geq 100\%$ was also compared between fuels, without corrections for atmospheric conditions. Mean RH_{ICE} was greater for LT PNNL fuel than for JetA1 (129% *c.f.* 117%) and thus set lower-bounds to the reductions in AEI for LT PNNL: AEIn, a reduction of >50% and possibly 80% by PPL fit; AEim, a reduction >31% and possibly 20% by PPL fit; for optical depth AECzy, a reduction of >27% and possibly 50% by PPL fit.

5.1.6 Median contrail cross-sectional spectral size of ice particles exhibited non-linear and multi-modal behaviour with T_S and RH_{ICE}. Size appeared to have increased marginally, 9%, under comparison of $RH_{ICE} \geq 100\%$ sub-sets, possibly 50% under comparison of AEIn and AEIm for LT PNNL, assuming sphericity.

5.1.7 For future research, it is highly desirable to conduct similar flights with additional instrumentation, namely a co-located extinction probe, so that the total Optical Depth can be measured directly, rather then the FSSP optical depth be derived by calculation for assumed-spherical ice particles > 0.5 µm only.

Classification: Unclass
Distribution: Unlimited

5.1.8 This would provide a robust data-set useful for conducting studies of contrail radiative effects, for a variety of radiation angles, in order to finally derive experimental values of the effects on high-blend biofuels upon RF.

ACKNOWLEDGEMENTS

Project CAAFCEB, flight research of contrails high-blend bio-jet fuels, acknowledges gratefully the sponsorship of Environment & Climate Change Canada, Transport Canada and the National Research Council Canada.

REFERENCES

1. Brown, A.P., Bastian, M., Pryor, M., Talgoy, P., "NRC CT-133 ACCESS II DATA ANALYSIS:- GASEOUS, AEROSOL AND CONTRAIL CHARACTERISTICS**,"** Flight Research Laboratory, NRC IFAR NASA ACCESS II Data Workshop, Kissimmee, FL, 9th January 2015
2. Brown, A.P., Bastian, M., Alavi, S., Wasey, M., "FLIGHT RESEARCH REPORT:- PROJECTS AEAFFR, CAAFER AND NASA ACCESS II JET TRANSPORT EMISSIONS MEASUREMENTS,' NRC LTR-FRL-2015-0054, March 2015.
3. Brown, A.P., Bastian, M. and Smallwood, G., "Aviation Emissions Index Derivation Methodologies from Flight Data, including Black Carbon and Aerosols," AIAA 40th Atmospheric and Space Environments Conference, New Orleans, 25-28 June 2012, AIAA-2012-2926.
4. Brown, A.P., Bastian, M., "Civil Aviation Alternate Fuels Contrails and Emissions Research (GARDN CAAFCER) – Contrails Analysis," NRC LTR-FRL-2018-0014, February 2018.
5. Environment Branch of the International Civil Aviation Organisation, "ICAO Environmental Report 2016, Aviation and Climate Change."
6. Korolev, A, Shashkov, A. and Barker, H., "Calibrations and Pereformance of the Airborne Cloud Extinction Probe," J.Atmos. & Ocean Tech., V0l.31, pp 326-344, February 2014. DOI10.1175/JTECH-D-13-00020.1.
7. LT PNNL fuel analysis test report.
8. Chan, T.W., Canteenwalla, P., Chishty, W. W., "GT2017-63131, Characterisation of Fuel Composition and Altitude Impact on Gaseous and Particle Emissions from a Turbojet Engine," Proceedings of ASME Turbo Expo 2017, , GT2017, 26-30 June 2017, Charlotte, NC, USA.

9. Miake-Lye, R. C., *et al*, "SO_x oxidation and volatile aerosol in aircraft exhaust plumes depend on fuel sulphur content, G.R.L., Vol.25, No.19, pp 1670-1680, 15 May 1998.
10. Karcher, B., "The importance of contrail ice formation for mitigating the climate impact of aviation," Journal of Geophysical Research: Atmospheres, 10.1002/2015JD024696, 2016, *pp* 3497-3505.
11. Moore, R.H. *et al*, "Biofuel blending reduces particle emissions from aircraft engines at cruise conditions," Nature, doi:10.1038/nature21420, 2017.
12. Poitras, P., "NRC Biofuel Flight Program Sample Testing," QETE 19100-1 (H001917), 21 July 2017, Quality Engineering Test Establishment, DND.
13. P. Jeßberger, C. Voigt, U. Schumann, I. Sölch, H. Schlager, S. Kaufmann, A. Petzold1, D. Schäuble, and J.-F. Gayet, "Aircraft type influence on contrail properties," Atmos. Chem. Phys., 13, 11965–11984, 2013 www.atmos-chem-phys.net/13/11965/2013/ doi:10.5194/acp-13-11965-2013.
14. Poitras, P., "NRC Biofuel Flight Program – Alcohol to Jet Fuel Sample Testing," QETE 19100-1 (H016517), 17 May 2018, Quality Engineering Test Establishment, DND.